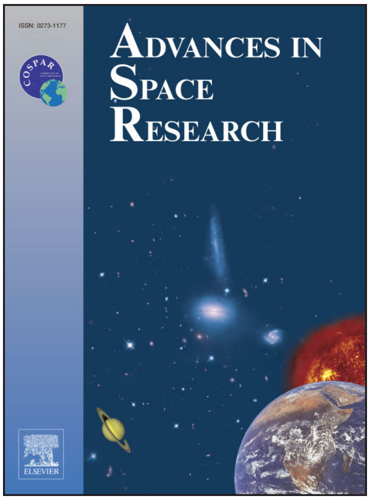

Space waste: An update of the anthropogenic matter injection into Earth's atmosphere

Leonard Schulz, Karl-Heinz Glassmeier, Moritz Herberhold, Adam Mitchell, Daniel M. Murphy, John M. C. Plane, Ferdinand Plaschke

PII: S0273-1177(26)00350-9
DOI: https://doi.org/10.1016/j.asr.2026.03.026
Reference: JASR 19420

To appear in: *Advances in Space Research*

Received Date: 23 October 2025
Revised Date: 9 January 2026
Accepted Date: 6 March 2026

Please cite this article as: Schulz, L., Glassmeier, K-H., Herberhold, M., Mitchell, A., Murphy, D.M., C. Plane, J.M., Plaschke, F., Space waste: An update of the anthropogenic matter injection into Earth's atmosphere, *Advances in Space Research* (2026), doi: https://doi.org/10.1016/j.asr.2026.03.026

Available online at www.sciencedirect.com

ScienceDirect

Advances in Space Research xx (2026) xxx-xxx

ADVANCES IN SPACE RESEARCH
(a COSPAR publication)

www.elsevier.com/locate/asr

Space waste: An update of the anthropogenic matter injection into Earth's atmosphere

Leonard Schulz[a,*], Karl-Heinz Glassmeier[a,b], Moritz Herberhold[c], Adam Mitchell[d], Daniel M. Murphy[e,f], John M. C. Plane[g], Ferdinand Plaschke[a]

[a] *Institute of Geophysics and Extraterrestrial Physics, Technische Universität Braunschweig, Braunschweig, 38106, Germany*
[b] *Max-Planck-Institute of Solar System Science, Göttingen, 37077, Germany*
[c] *German Aerospace Center (DLR), Bremen, 28359, Germany*
[d] *European Space Agency (ESA), European Space Research and Technology Centre, Noordwijk, 2200 AG, Netherlands*
[e] *Chemical Sciences Laboratory, National Oceanic and Atmospheric Administration, Boulder, CO, 80305, USA*
[f] *Purdue University, West Lafayette, IN, 47907, USA*
[g] *University of Leeds, Leeds, LS2 9JT, United Kingdom*

Abstract

Large satellite constellations are one of the main reasons for an increasing amount of mass being brought into low Earth orbit in recent years. After end of life, the satellites, as well as rocket stages, reenter Earth's atmosphere. This space waste burns up in the atmosphere and thus injects a substantial amount of its matter into the mesosphere and lower thermosphere. A first comprehensive analysis of the anthropogenic injection and a comparison to the natural injection by meteoroids was presented by Schulz & Glassmeier (2021) (Advances in Space Research, 67 (3), 1002-1025). They found significant and even the dominant injection of several metal elements regularly used in spacecraft compared to the natural injection. The first observations of space waste remnants in stratospheric aerosol particles (Murphy et al., 2023, PNAS, Vol. 120, No. 43, e2313374120) confirmed several of these estimates, but also revealed differences and new insights: in particular, a much more extensive range of elements. These inventories and observations raise questions of possible environmental effects, especially on the stratospheric ozone layer (Mitchell et al., 2024, Understanding the Atmospheric Effects from Spacecraft Re-entry, ESA, Whitepaper, 2024). The current study presents an update to the space waste injection estimates of Schulz & Glassmeier (2021), assessing the years from 2015 to 2025 using available reentry databases but also considering future mass influx scenarios. Combining mass influx data with detailed estimates of average satellite and rocket stage composition as well as ablation factors allows the estimation of the mass injection of 43 elements and thus a much more detailed comparison to the meteoric injection. Comparison of estimated elemental fluxes to stratospheric aerosol data shows excellent agreement. In general, from 2020 onward, a strong rise in space waste mass influx to the atmosphere can be seen, which has led to more than double the atmospheric injected mass in 2024 compared to levels from 2015 to 2020. Future scenarios discussed by Schulz & Glassmeier (2021) may already be reached by the end of 2025. In 2024, 24 elements were dominating the meteoric injection compared to 18 in 2015, this might increase to 30 in the future. Several of them are transition metals, which are known for their catalytic activity. This indicates a substantial risk of long-term adverse effects on the atmosphere such as ozone depletion, radiative effects and changes in cloud formation, if no action is taken. Research is urgently needed into the atmospheric accumulation, chemistry, and general atmospheric effects of specific elements.

Keywords: Atmosphere ; Satellite constellations ; Ablation ; Space debris ; Anthropogenic effect

---

[*] Corresponding author.

Email addresses: `l.schulz@tu-bs.de` (Leonard Schulz), `kh.glassmeier@tu-bs.de` (Karl-Heinz Glassmeier), `moritz.herberhold@dlr.de` (Moritz Herberhold), `adam.mitchell@ext.esa.int` (Adam Mitchell), `daniel.m.murphy@noaa.gov` (Daniel M. Murphy), `j.m.c.plane@leeds.ac.uk` (John M. C. Plane), `f.plaschke@tu-bs.de` (Ferdinand Plaschke)

https://dx.doi.org/10.1016/j.jasr.xxxx.xx.xxx

1. Introduction

The marked increase in space activities in the past 5 years has led to a strong rise in mass that is entering into orbit. The main driver is large satellite constellations with thousands of satellites already launched, and tens- to hundreds of thousands being planned. All in all, more than a million constellation satellites are proposed (Falle et al., 2023). This leads to three different sustainability problems of spaceflight:

1. *Space debris* is "artificial material that is orbiting Earth but no longer functional" (Gregersen, 2025b). It is a long-known problem (Kessler & Cour-Palais, 1978; Klinkrad, 2006) posed by satellites and rocket stages staying in orbit after their end of life. The largely increased number of objects, especially in orbital shells occupied by large satellite constellations, increases the risk of collisions. In the worst case, this leads to the Kessler syndrome, in which a long-term chain reaction of collisions can render entire orbital shells unusable. This issue is being addressed by space agencies, which project worsening conditions even if no further launches were to take place (ESA Space Debris Office, 2025). For LEO (Low Earth Orbit), the only viable mitigation option is the reentry of an object into the atmosphere. This leads to another problem, namely
2. *Ground impacts*. Parts of satellites and rocket bodies can survive destructive reentry (e. g. Ailor et al., 2005) and end up on the ground. As the number of reentering objects rises, the total risk of a deadly event increases as well (Pardini & Anselmo, 2025). To minimize this risk, efforts are being made toward complete demise of spacecraft upon atmospheric reentry. This risk minimization amplifies the third problem, namely
3. **Space waste**, which we define as all artificial material — fragmented or intact, from orbital or suborbital trajectories — (re-)entering Earth's atmosphere and undergoing destructive ablation. This includes for example suborbital rocket stages and fragmentation debris that ablate in the atmosphere. Space waste releases considerable amounts of vapor and particulates into the upper atmosphere. We use the term space waste to contrast with the well-known problem of space debris, which solely constitutes an in-orbit hazard. Space waste on the other hand has effects on Earth's atmosphere.

The atmospheric influence from space waste reentry has long been regarded as negligible (Lohn et al., 1994; Smith et al., 1999; Bianchi, 2019; Toumi, 2019). However, Schulz & Glassmeier (2021) showed that the mass annually injected to the atmosphere is already significant compared to the natural input by ablation of meteoroids and can even dominate for some metals like Al or Cu. Measurements of space waste remnants in stratospheric aerosol particles (Murphy et al., 2023) largely confirmed these estimates and also showed Li and Pb dominating. A significance or dominance compared to natural levels inevitably poses the question of possible environmental effects. This is especially true for Earth's atmosphere due to the complexity of the system: the same constituent can have different effects in different atmospheric layers. Space waste can start ablating at altitudes as high as 110 km and ablation may last down to 40 km (Yamauchi et al., 2024, and references therein). However, the majority of the material is injected into the mesosphere (50 to 85 km), where it is expected to mix with the meteoroid background to form aerosol particles. Mesospheric circulation transports these aerosols to the winter poles, where they descend toward the stratosphere and can be measured (Murphy et al., 2023). While the complex metal chemistry in the mesosphere and lower thermosphere has been extensively modeled and validated by measurements of metals injected by meteoroids (e. g. Feng et al., 2013; Mangan et al., 2020; Plane et al., 2021), the wide variety of space waste metals that have low abundances in meteoroids as well as the lower ablation altitudes mean that new chemistry is expected in the mesosphere and stratosphere. The new materials can potentially foster polar mesospheric cloud and polar stratospheric cloud nucleation, allow new paths of heterogeneous chemistry in the stratosphere that could catalytically destroy ozone, influence radiative forcing and produce particles with unusual optical properties (Schulz & Glassmeier, 2021; Boley & Byers, 2021; Shutler et al., 2022; Murphy et al., 2023; Mitchell et al., 2024). There is therefore a wide variety of possible effects that could induce long-term changes of the atmosphere. If mass is ablated above 80 km, influences and contribution to the ionosphere and even magnetosphere are possible (Yamauchi et al., 2024). Modeling studies have started to shine light on the implication of the atmospheric injection, focusing on effects of future elevated aerosol emissions (Jain & Hastings, 2025; Maloney et al., 2025), and giving insights into the molecular scale demise process (Ferreira et al., 2024). Other studies have addressed the issue of space waste matter injection together with exhaust from rocket launches (e. g. Miraux, 2022; Ryan et al., 2022; Fischer & Fasoulas, 2024), and tried to work out a complete life cycle assessment of space activities (e. g. Miraux et al., 2022).

Beside the space waste injection estimation that addressed 10 different elements by Schulz & Glassmeier (2021), other estimates have mainly focused on the aluminum input (Ferreira et al., 2024; Barker et al., 2024; Fischer & Fasoulas, 2024). Earlier studies (Bianchi, 2019; Toumi, 2019) give more elaborate injection estimates but the origin of the data is unclear. The first observations of space waste remnants in the stratosphere (Murphy et al., 2023) have confirmed many of the estimates made in Schulz & Glassmeier (2021), such as the relative input of Al to Cu, the wide variety of materials being injected into the atmosphere, and the anthropogenic fraction of Al. However, there are also considerable differences, and for some metals detected by Murphy et al. (2023), no injection values were estimated. Also, the past few years have already shown a significant increase in launch activity: there are nearly 10,000 large constellation satellites in orbit. With the first significant batches of constellation satellites being launched in 2020, and a typical lifetime of 5 years, we are now seeing the start of frequent reentries of these constellation satellites, in addition to the already high influx numbers.

This study presents an update to the atmospheric injection of space waste presented by Schulz & Glassmeier (2021). Injection estimates for the years 2015 to 2025, as well as two future scenarios for 43 elements, are determined by using reentry databases, extending rocket stage knowledge and improving the estimation of the average elemental composition of satellites and rocket stages. To show the significance of the anthropogenic injection as well as to highlight essential future research paths, the resulting estimates are compared to both the natural influx and analyses of stratospheric aerosol particles (Murphy et al., 2023).

2. Anthropogenic injection

As in Schulz & Glassmeier (2021), we estimate the space waste injection into Earth's atmosphere from the mass influx to the top of the atmosphere, the space waste elemental mass composition, and the ablation fraction. By combining this information, insights into the total and elemental annual injection rates are obtained.

2.1. *Mass influx*

2.1.1. *Data origin*

The space waste mass influx can be divided into orbital and suborbital objects reentering the atmosphere. Nearly all orbital objects are either satellites or rocket upper stages; a comparably small amount of mass is debris such as payload adapters, solar panel covers or disintegration remnants. We group them together with satellites. The annual mass influx of satellites and upper stages is obtained from the Catalog of Space Object Reentries of "Jonathan's Space Report" (McDowell, 2025c), where we exclude all entries labeled suborbital (tagged D-SO), having left Earth's sphere of influence (U-HEL and D-LUN) and designed to land (D-LAND). The latter for example include manned return capsules (Soyuz-MS, Crew Dragon, Shenzhou, Orion), reconnaissance satellites (Yantar-4K2M) or unmanned return vehicles (X-37B, Chongfu Shiyong Shiyan Hangtian Qi, Cargo Dragon 2, Shi Jian 19). The upper stages of test flights 2, 7, and 8 of SpaceX's Starship are added due to their large mass reaching close to orbital velocity and observations of their destructive reentry. While there is a generally good agreement between McDowell (2025c) and ESA's DISCOS database (ESA, 2025), we opt for the former as more realistic dry masses are provided and additional objects (such as separated service modules of reentry vehicles) are included.

Suborbital objects are mainly rocket core stages which are jettisoned before reaching orbit. Thus, they reenter the atmosphere directly after their ascent with speeds ranging from 2 (when jettisoned early-on) to 8 km/s (close to orbital speed). If the velocity is high enough, they too ablate upon re-entry. We adopt a threshold velocity of 3.8 km/s from Schulz & Glassmeier (2021), which corresponds to about a quarter of the kinetic energy of a typical orbital reentry. Below that, we expect no significant ablation and thus disregard all booster stages (strap-on rocket boosters), nearly all payload fairings, and all purely suborbital launches (such as ICBM tests or sounding rockets). We also disregard suborbital rocket stages designed for reuse such as the Falcon 9/Heavy or Starship core stages. Orbital rocket launches are obtained from DISCOS (ESA, 2025) with the dry masses gathered from Barker et al. (2024); Schulz & Glassmeier (2021); Krebs (2025); McDowell (2025b), or estimated using launch data. Reentry velocities at 100 km altitude are either taken from Schulz & Glassmeier (2021), calculated from trajectory data, or determined from launch coverage. A detailed list of the relevant core stages and their typical reentry velocities is provided in Appendix A.

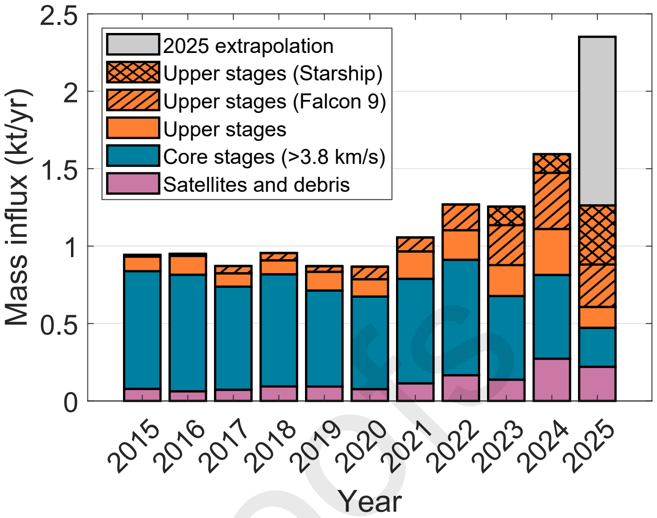

Fig. 1. Annual mass influx to the top of the atmosphere (meaning before ablation), with differentiation of object type. The gray bar shows the mass influx expected for the rest of 2025 when extrapolating the current numbers (until July 16th 2025) to the end of year.

2.1.2. *Historical reentry data (2015–2025)*

Using the above described datasets, we determine the annual mass influx to the top of the atmosphere (prior to ablation) for the years 2015 to 2025 (until July 16th, 2025). We differentiate between satellites, rocket upper stages and (suborbital) core stages in order to account for their different composition and ablation fraction. Additionally, we divide upper stages into three categories — Falcon 9/Falcon Heavy, Starship, and all others — because of additional composition data available and significant mass contributions in recent years for the first two (especially Starship with 120 t to 127 t of mass per stage depending on the version). The mass influx is depicted in Figure 1 and Table 1, including an extrapolation to the end of 2025 assuming the same rate of influx as earlier in the year. While the annual mass influx has been more or less constant just below 1 kt/yr for the years 2015 to 2020, with the onset of the first large satellite constellations, it has increased since 2020 to 1.6 kt in 2024 and (considering the extrapolation) above 2.3 kt

Table 1. Annual space waste mass influx to the top of the atmosphere (meaning before ablation), with differentiation by object type. All values in kt/yr. Uncertainties of the total mass influx are at 3% (see Section 2.4) and represent 3σ uncertainties.

Year	Satellites and debris	Core stages	Upper stages	Upper stages (only Falcon 9/Heavy)	Upper stages (only Starship)	Total
2015	0.08	0.76	0.11	0.01	0.00	0.94 ± 0.03
2016	0.06	0.75	0.14	0.01	0.00	0.95 ± 0.03
2017	0.07	0.67	0.13	0.05	0.00	0.87 ± 0.03
2018	0.09	0.72	0.14	0.05	0.00	0.96 ± 0.03
2019	0.09	0.62	0.16	0.04	0.00	0.87 ± 0.03
2020	0.08	0.60	0.19	0.08	0.00	0.87 ± 0.03
2021	0.11	0.68	0.27	0.09	0.00	1.06 ± 0.03
2022	0.17	0.75	0.36	0.17	0.00	1.27 ± 0.04
2023	0.14	0.54	0.58	0.26	0.12	1.26 ± 0.04
2024	0.27	0.54	0.78	0.36	0.12	1.59 ± 0.05
2025 (until July 16th)	0.22	0.25	0.79	0.27	0.38	1.26 ± 0.04
2025 (whole year, extrapol.)						2.35

in 2025. It is quite clear that the increase is mainly attributable to the increased large satellite constellation activity, mainly due to Starlink. This can be seen from the continuous increase in Falcon 9 upper stages reentering annually (they are often used to put Starlink satellites into orbit) and also the increasing number of reentering Starlink satellites (Oliveira et al., 2025). With their typical lifetime of 5 years, we are just at the start of drastically increased reentry numbers of large constellation satellites.

2.1.3. *Future scenarios*

Since 2020, the number of proposed satellites in large constellations has increased from 110,000 (Schulz & Glassmeier, 2021) to more than a million (Falle et al., 2023). However, many of the currently proposed large satellite constellations are unlikely to be realized (Falle et al., 2023). In some cases, applications might be based on the intent to sell the blocked part of the spectrum later on, rather than an actual desire to install the proposed constellation. Therefore, contrary to the approach by Schulz & Glassmeier (2021), it is now more prudent to base future scenarios on the number of satellites within constellations that are actually being launched. The number of launched satellites in large constellations rose unprecedentedly from zero in 2019 to nearly 10,000 at the end of 2025 (McDowell, 2025a). At present, these are nearly all either Starlink or OneWeb. The Chinese constellations Guowang and Qianfan as well as Amazon's Kuiper constellation are starting to be launched, with tens of satellites each already in orbit (Gregersen, 2025a). While the OneWeb constellation is completed at about 650 satellites, current deployment plans are at 30,000 to 42,000 satellites for Starlink, 3,200 for Kuiper, 13,000 for Guowang and 15,000 for Qianfan. At maximum, these currently installed constellation would thus sum to nearly 74,000 satellites.

Based on this, we reuse the scenarios by Schulz & Glassmeier (2021). Their "probable" scenario 1 of 19,400 satellites in active constellations represents a doubling compared to the current number and can now be described as likely to be reached within the coming years. Their scenario 2 with 75,000 constellation satellites represents a full completion of the large constellations currently in active deployment and is no longer a "worst-case scenario" but probable to be reached. The adopted two future scenarios represent an annual mass influx of 2.7 and 8.1 kt, respectively.

2.2. *Composition*

The composition of satellites and rocket bodies is (in many cases) proprietary knowledge of manufacturers and operators. Therefore, detailed composition information about specific launch vehicles or spacecraft is hard to obtain. Here, we combine information from space material databases with anonymized manufacturer data, institution and industry reports, and available scientific literature, to obtain a fairly complete picture of components and materials and their relative mass fractions. Through datasheets, other literature, and stoichiometry of used chemicals, the elemental mass composition of each component or material is determined. Combination of all the acquired information yields average elemental mass compositions of satellites, the different upper stages, and core stages, given in Appendix B. These are significantly improved compared to the rough estimates presented by Schulz & Glassmeier (2021) and allow for credible mass fractions for a high number of elements besides the commonly considered aluminum (e. g. Barker et al., 2024; Fischer & Fasoulas, 2024; Ferreira et al., 2024).

The main sources we have used are "SPACEMATDB — Space Materials DataBase" (de Rooij), which combines data from several sources, and the Aerospace Structural Metals Handbook (Gunderson et al., 2007). They include information about typical alloys and other materials used, datasheets, and general application areas of the materials as well as usage in certain launch vehicles and spacecraft.

For both satellites and rocket stages we neglect residual propellant as all relevant space agencies require depletion through venting or depletion burns after the end of mission (Inter-Agency Space Debris Coordination Committee, 2025). Although a small fraction of satellites fail after orbit insertion (Xu et al., 2023) and this releases larger amounts of propellant upon re-entry, the failure rate combined with typical fuel load (Wertz et al., 2011) points towards negligible amounts being injected into the stratosphere when comparing to the annual space waste mass influx.

2.2.1. Satellite composition

Satellites re-entering Earth's atmosphere are predominantly from LEO. A large European satellite manufacturer (LSI) provided an anonymized dataset, which lists the mass fraction of material groups (according to the ECSS-Q-ST-70 material classification, ECSS Secreteriat, 2019) of a typical LEO satellite (less than 1 ton dry mass) based on a metal structure. We combine this data with mean satellite compositions given in the ATISPADE (Toumi, 2019) and ARA studies (Grassi, 2017; Bianchi, 2019), as well as by Beck et al. (2019). For these studies, single materials are provided rather than material groups (e. g. copper instead of its material group copper alloys). We allocate the materials to the appropriate material groups if possible, in order to reach mass fractions for each material group. Depending on the maturity of the data, we chose a mean value of all studies or took values from only a subset of studies to reach an average mass fraction for each material group. However, the material groups do not include (or only partially include) components like PCB (printed circuit board) electronics, batteries, solar cells, and CFRP (carbon fibre-reinforced polymer). As these components are significant contributors especially regarding specific metallic elements, we estimate them separately. While CFRP can be estimated using the data from all four datasets, the other components are not listed consistently and the values that are presented seem to be zero-order estimates with unlikely values. Thus, different sources are used to assess the mass fraction of these components. The final mass fractions of each material group are obtained by renormalizing all other obtained mass fraction values so that a 100% total is reached.

Representative materials of each group are then found by combining data provided by the LSI, an ESA (European Space Agency) materials list, (de Rooij) and datasheets. Mass fractions of these representative materials within each material group are either calculated or based on the frequency of use reported; a complete list is provided in Appendix C. Table 2 shows the material groups/components together with the associated mass fraction, the source of the mass fraction and typical, representative materials. In the following, the components respectively material groups will be discussed individually. Sources of the elemental mass composition of typical materials are given in parenthesis when they are first mentioned. If no source is mentioned, the composition is taken from de Rooij.

Aluminum, aluminum alloys and CFRP. Aluminum alloys are predominantly used in structures, with CFRP gaining more and more ground. The link between structural application and mass fraction can also clearly be seen from the LSI data, which shows no or very little use of CFRP while the typical satellite assumed by Toumi (2019); Beck et al. (2019) attributes 25% of the satellite mass to CFRP. This reduces the Al alloy portion from 54% in the LSI data to 27 and 35% in Toumi (2019) and Beck et al. (2019), respectively. The values by Grassi (2017) are in between, for both CFRP and Al alloys. For both Al alloys and CFRP, we have taken the average value of all 4 studies.

Common Al alloys in use are 7075 (Alcoa Mill products), 2024, 6061, and 5052 (de Rooij). We attribute 40% of the Al alloy mass to the most commonly mentioned 7075 and the remaining 60% equally shared between the other three alloys.

CFRP is made of carbon fibres which are embedded in an exopy or cyanate ester resin. Typically, the carbon fibres make up about 60% of the material (Sun et al., 2015; Bonvoisin et al., 2023). Epoxy resin CFRP is still more widely in use (we assume 60%) compared to cyanate ester resin CFRP (the remaining 40%). For epoxy resin CFRP, we use the mean of XPS analysis performed by Sun et al. (2015); Metzler et al. (2016); Wen et al. (2024) assuming volume fractions to be reasonably close to mass fractions and accounting for the missing hydrogen with 3.2% of the total mass. Besides the usual organics, a small portion of chlorine (<1%) remains in the epoxy resin due to incomplete synthesis of epichlorohydrine. For cyanate ester resins, we assume bisphenol A dicyanate in a matrix together with the typical triazin repeating unit (Meier, 2021; Daken Chemical, 2024). Stoichiometry yields the elemental mass composition.

Other alloys and metals. Copper, nickel, titanium and their alloys as well as steels, stainless steels and other metallic elements are found in various different applications such as structural elements, fuel tanks, electronic assemblies, nozzles and thrusters, actuators, bearings, thermal systems, plating and other applications. For details on the applications, the reader is referred to de Rooij; Finckenor (2018). Common alloys and metal types in use are obtained from the material list from the LSI, the ESA materials list and de Rooij. For copper and its alloys, we assume an equal share of pure Cu, bronze (CDA 510), Ni-Al-bronze (CDA 632 and C95500 (Wieland Concast, 2025)), brass (CDA 230 and CDA 260), and $CuBe_2$ (Metalcor GmbH, 2025b) coated with 0.5% of Ag and Au. For nickel, we assume an equal share of pure Ni and Invar; for titanium, Ti6Al4V (SLM Solution Group Ag, 2019) and Ti3Al2.5V are equally frequent in use. For steels, an equal fraction of 4130 and 4340 (pauly Stahlhandel GmbH & Co. KG, 2025) is assumed and for stainless steel we assume 50% of mass shared equally between the common 301, 304L (AK Steel Corporation, 2007c) and 316L alloy types, 30% of 431 and 10% each of the specialized A286 (ATI, 2012) and 17-4PH (Stahlhandel Gröditz GmbH) stainless steels.

Filler metals, welding, brazing, soldering. Here, solder is the major component. While efforts are being made to move to lead-free solder, typical solder with 40% Pb and 60% Sn is still widely in use (de Rooij; ELSOLD).

Optical materials. Typical glasses used are BK7 and ZERODUR. These consist mainly of silica (SiO_2) combined with other metal oxides such as B_2O_3, ZnO, Al_2O_3, Na_2O, TiO_2, K_2O, ZrO_2, MgO, P_4O_{10}, Li_2O, BaO and trace amounts of CaO and As_2O_3. Approximate compositions are given in Newport Glass Works, Ltd. (2015a,b). Fused silica glass consisting

Table 2. Estimated average composition of a LEO satellite. The mass fractions refer solely to the respective material groups, not elemental composition. Typical materials used for modeling of an average satellite composition are given in the fourth column. The fractions of the typical materials within each material group are provided in Appendix C.

Material groups	Mass fraction (%)	Source of mass fraction	Typical materials	References
Aluminum and aluminum alloys	36.7	Mean of LSI, Toumi (2019); Grassi (2017); Beck et al. (2019)	7075, 2024, 6061, 5052	LSI list; Bonvoisin et al. (2023); de Rooij; Lerch (2018); Alcoa Mill products; thyssenkrupp Materials Services GmbH (2018)
CFRP	15.1	Mean of LSI, Toumi (2019); Grassi (2017); Beck et al. (2019)	Carbon fibre + epoxy resin or cyanate ester resin	Sun et al. (2015); Bonvoisin et al. (2023); Metzler et al. (2016); Wen et al. (2024); Meier (2021); Daken Chemical (2024)
Copper and copper alloys (not including copper in other materials)	1.4	LSI	Cu, bronze (CDA 510), Ni-Al-bronze (CDA 632, C95500), brass (CDA 230, CDA 260), $CuBe_2$ with coating of Ag or Au	LSI list; de Rooij; Wieland Concast (2025); Metalcor GmbH (2025b)
Nickel and nickel alloys	0.5	Mean of LSI, Toumi (2019); Grassi (2017); Beck et al. (2019)	Ni, Invar	LSI list; de Rooij
Titanium and titanium alloys	4.6	Mean of LSI, Toumi (2019); Grassi (2017); Beck et al. (2019)	Ti6Al4, Ti3Al2.5V	LSI list; de Rooij; Bonvoisin et al. (2023); SLM Solution Group Ag (2019)
Steels	0.1	LSI	4130, 4340	de Rooij; pauly Stahlhandel GmbH & Co. KG (2025)
Stainless steels	3.2	Mean of LSI, Toumi (2019); Grassi (2017); Beck et al. (2019)	431, 301, 304L, 316L, A286, 17-4PH	LSI list, ESA list, de Rooij; AK Steel Corporation (2007c); ATI (2012); Stahlhandel Gröditz GmbH
Welding, brazing, soldering	1.1	Mean of LSI, Toumi (2019); Grassi (2017); Beck et al. (2019)	SnPb (solder)	LSI list, Kester (2016)
Miscellaneous metallic materials	0.4	Mean of LSI, Toumi (2019); Grassi (2017); Beck et al. (2019)	AZ31B	de Rooij
Optical materials	2.9	Mean of LSI, Toumi (2019); Grassi (2017); Beck et al. (2019)	BK7, ZERODUR, SiO_2	LSI list, Newport Glass Works, Ltd. (2015b,a)
Adhesives, coatings, varnishes	5.4	LSI	Acrylate, silicone, epoxy	LSI list, de Rooij; Henkel Limited (2015); DOW CORNING (2011); 3M (2008); National Starch & Chemical Company (2004)
Adhesive tapes	1.6	LSI	Acrylate	LSI list
Paints, primers and inks	0.5	LSI	PU + black carbon, silicone + ZnO	LSI list, de Rooij; LORD Corporation (2013); Lecadre-Scotto et al. (2025); Kayhan et al. (2012)
Lubricants	< 0.1	Mean of LSI, Toumi (2019); Grassi (2017); Beck et al. (2019)	MoS_2, PFPE	LSI list, de Rooij
Potting compounds, sealants, foams	1.9	LSI	PU, silicone, epoxy	de Rooij; Emerson & Cuming Microwave Products, Inc. (2011); NuSil Technology LLC (2009); Chawla (2001); Henkel Corporation (2023)
Rubbers and elastomers	0.2	Mean of LSI, Toumi (2019); Grassi (2017); Beck et al. (2019)	Viton B910, nitrile butadiene rubber	LSI list, de Rooij; Barber (2001); Trelleborg sealing solutions Germany GmbH (2025)
Thermoplastics (non-adhesive tapes and foils, e. g. MLI)	3.7	LSI	Polyimide, polyolefin, DACRON, PTFE, PEEK, PVDE	de Rooij; Shu et al. (2016); Goodfellow GMBH (2024)
Wires and cables	7.2	Mean of LSI and Toumi (2019)	Cu, PTFE, PFA, polyimide, Ag	GORE (2016)
Miscellaneous non-metallic materials (e. g. ceramics)	1.0	LSI	Al_2O_3, Si_3N_4, AlN, SiC	LSI list, Bonvoisin et al. (2023)
Electronics (PCBs)	5.0	Wertz et al. (2011)	Polyimide, FR4, electronic elements	Korf et al. (2019); Mumby (1989); de Rooij
Li-ion Batteries	6.4	Calculated using (Wertz et al., 2011), other sources (see text)	Al, Cu, $LiPF_6$, $LiCoO_2$, $LiNi_{0.84}Co_{0.12}Al_{0.04}O_2$, graphite, C_2H_4	Ehrlich (2001); Borthomieu (2014); Pathak et al. (2023); GS Yuasa Power Supply Ltd.; GS Yuasa Lithium Power, Inc.; Borthomieu et al. (2019); Saft (2020)
Solar cells + cover glass	1.0	Calculated assuming $10\,m^2$ of solar array	CMX100 cover glass, triple junction solar cells substrate (InGaP/GaAs/Ge), silicon solar cell substrate	AZUR SPACE Solar Power GmbH (2016a,b,c); SHARP (2023); Lin et al. (2016); Li et al. (2021); QIOPTIQ; Kearsley et al. (2007)
Total	100.0			

purely of silica is used as well. We assume equal mass fraction of these three kinds of glasses. Solar cell cover glass is addressed under solar panels below.

Adhesives, coatings, varnishes and adhesive tapes. We group these into acrylate, silicone and epoxy based, assuming equal mass fraction for each type. Approximate chemical compositions of representative substances are available in Henkel Limited (2015) for an acrylic adhesive, in DOW CORNING (2011) for a silicone varnish, and in 3M (2008); National Starch & Chemical Company (2004) for two epoxy adhesives; the latter being electrically conducting due to a high silver content. For the epoxy resin itself, we assume Bisphenol A diglycidyl ether, as it is commonly used for epoxy resins. As with the CFRP epoxy resins, we assume proportionate trace amounts of chlorine in the epoxy resin due to incomplete synthesis of epichlorohydrine.

For adhesive tapes, no chemical composition of a representative product could be found. As acrylate is used, we assume the same composition as for the acrylate adhesive.

Paints, primers and inks. Both polyurethane (PU) and silicone based paints are used. We assume an equal share of a black, PU based paint and a white, silicone based paint as these are commonly used (de Rooij) as both heating and cooling may be needed in the LEO environment. A representative chemical composition of a black paint with black carbon as pigment is obtained from LORD Corporation (2013), assuming the ester solvents as butyl acetate. White paints normally contains ZnO as the pigment; we assume polydimethylsiloxane (PDMS) as the silicone binder (Lecadre-Scotto et al., 2025) and the ZnO mass fraction to be 27% (Kayhan et al., 2012). For both, the elemental mass composition is determined through stoichiometry.

Lubricants. While lubricants only make up a very small overall mass fraction of a satellite, we model them as the dry lubricant MoS_2 and perfluoropolyether (PFPE). The elemental mass compositions are determined via the stoichiometric ratios, assuming a reapeating unit of C_2F_4O for PFPE.

Potting compounds, sealants, foams. Taking acount of the materials described in de Rooij, we assume an equal share of PU foam, epoxy and silicone based materials. Again, representative materials are chosen from datasheets. For PU foam, we model the composition after Emerson & Cuming Microwave Products, Inc. (2011) with 60% Toluene-2,4-Diisocyanate (TDI) and the rest an isocyanate terminated polymer (dipropylen glycol). For silicone, we choose NuSil Technology LLC (2009), which contains 20% silica and 15% 2-Butanone, 0,0',0" (methylsilylidyne) trioxime, the rest is assumed to be silicon binder (PDMS, see above). Epoxy foam is modeled after Henkel Corporation (2023), assuming E-glass (21.5 wt%) being used (e. g. Chawla, 2001) and trace amounts of chlorine remaining from incomplete synthesis of epichlorohydrine (as above).

Rubbers and elastomers. Viton B910 as well as nitrile butadiene rubber (NBR) are used; we assume an equal share of mass. The former consists of vinylidene fluoride (1,1-Difluoroethylene) and a hexafluoropropylene copolymer (de Rooij) with the latter making up about 10% of the mass (Barber, 2001). NBR is derived from acrylonitrile (ACN) and butadiene, with ACN making up about 34% of the copolymer mass (Trelleborg sealing solutions Germany GmbH, 2025). Thus, both materials' elemental composition can be calculated using stoichiometry.

Thermoplastics (e. g. MLI). Here, we assume 70% of the mass being multi-layer insulation (MLI) with representative materials polyimide (namely Kapton, which is poly(4,4'-oxydiphenylene pyromellitimide, Shu et al., 2016), polyolefin (such as polyehtlyene (PE) or polypropylene (PP)) and polyethylene terephthalate (PET). The optical properties of MLI are normally achieved by a thin aluminized layer. Based on its thickness relative to the thickness of the whole sheet, we calculate the aluminum content to 0.03% (Goodfellow GMBH, 2024). The remaining 30% of the mass are attributed to polytetrafluoroethylene, polyether ether ketone and polyvinylidene fluoride.

Miscellaneous non-metallic materials. Here, ceramics such as alumina (Al_2O_3), silicon nitride (Si_3N_4), aluminum nitride (AlN) and silicon carbide (SiC) (Bonvoisin et al., 2023) are the dominating mass contributors. Assuming each to contribute a quarter of the mass, stoichiometry yields the elemental mass composition.

Batteries. Today's satellites almost exclusively use Li-ion batteries as they are superior to older battery types in various ways, e.g. specific energy and power density (Borthomieu, 2014; Pathak et al., 2023). Two types, namely LCO ($LiCoO_2$) and NCA ($LiNi_{0.84}Co_{0.12}Al_{0.04}O_2$), are used for the positive electrode (Borthomieu, 2014; GS Yuasa Power Supply Ltd.; GS Yuasa Lithium Power, Inc.; Borthomieu et al., 2019; Saft, 2020), while the negative electrode is normally graphite, along with a $LiPF_6$ electrolyte and polyolefin separator (Ehrlich, 2001). The relative mass contribution of the different constituents is known (Ehrlich, 2001). We assume the casing to be aluminium, the cap assembly to be copper, and the separator to be PE. Considering typical capacities needed for LEO satellites (100-150 Ah, cf. Wertz et al., 2011) and available datasheets of batteries for use in the LEO environment (Saft, 2020; Eaglepicher Technologies, 2022), battery mass is about 25 to 40 kg. Assuming a typical LEO satellite mass of about 600 kg, this translates to 4.0 to 6.4% of the satellite mass in batteries. Considering values of roughly 7.5% and 9.1% derived from mass budget information in Dudley &Verniolle (1997), and Wertz et al. (2011), respectively, we adopt the upper limit of 6.4%.

Electronics (PCBs). According to Wertz et al. (2011), the onboard computer generally makes up 5% of the mass of a satellite. We assume this to be only PCB mass. For its composition, we take the mean PCB composition from the literature review in Korf et al. (2019) and amend the data by the organic elements not analyzed (H, C, O). Those are determined from the elemental mass fractions of a FR4 PCB laminate material (Mumby, 1989), which is still commonly used today (e. g. de Rooij).

Wires and cables. For wiring and cables, a mean mass fraction of around 7 to 8% of the satellite mass is obtained from the LSI and Toumi (2019), consistent with the copper content given by Beck et al. (2019). While the majority of the material of a cable is copper, a substantial mass portion is insulation and jacket. Trace amounts of silver are used for better conduction. We use a data sheet from a major space cable distributor (GORE, 2016) giving detailed information about the thicknesses of the copper core, the very thin silver coating as well the insulation and jacket, which normally consist of PTFE, polyimide and PFA. We chose several shielded and non-shielded SPM cables and find an average of the copper (just above 50%), silver (below 1%) and plastic content. We assume half of the plastic content being PTFE, and a quarter PFA and polyimide, each.

Solar panels. We estimate the solar array size of a typical LEO satellite to be around $10\,\mathrm{m}^2$, based on the Iridium NEXT satellites (e. g. Eames, 2014). Solar arrays consist of the structure, wiring, the solar cell itself as well as cover glass. The former two are modeled separately (see above). The actual solar cells are extremely thin, as is the cover glass. Datasheets give values of the density of the whole assembly between 32 to $150\,\mathrm{mg/cm}^2$ (AZUR SPACE Solar Power GmbH, 2016a,b,c; SHARP, 2023), which translates to an average of 9.1 kg of solar cell and cover glass — about 1% of the satellite's mass. Appropriate values are 65% of the mass being solar cell material, and 35% cover glass.

Due to their superior efficiency, triple junction InGaP/GaAs/Ge solar cells are used much more frequently than the cheaper silicon-only cells. Based on the availability of datasheets and the present product palettes, we assume 80% being multi-junction solar cells. These exhibit a complex layering of differently doped substances with the majority of the mass being the Ge substrate. We model this layering after Lin et al. (2016); Li et al. (2021) and thus determine the elemental composition. For both cells, a silver layer is used for electric contact. The cover glass is normally borosilicate glass doped with cerium dioxide to shield from UV radiation (e. g. CMX, QIOPTIQ; Kearsley et al., 2007)). We model it after the cover glass of the Hubble space telescope (pers. comm. A. T. Kearsley, Natural History Museum, London, UK).

2.2.2. Average upper stage composition

We determine a typical upper stage composition by averaging component mass fractions of the AVUM stage of the Vega rocket (Dumon et al., 2022) and the Delta II upper stage (Lips et al., 2013; Steckel & Adams, 2018). The data is complemented by information obtained from Tizón & Roman (2017); Toumi (2019); Beck et al. (2019). Again, after averaging, we renormalize the total component mass fraction to 100%. Solid rocket motors are neglected as they are less commonly used in upper stages. In any case, they would not introduce different materials compared to liquid fueled rocket stages: paints and reaction control system components are similar, common steels and CFRP are used for structural components and nozzles, and insulation fibres and nozzle ablators are compositionally similar to CFRP (Henson, 2018; Trinh, 2018).

Common materials of rocket upper stages are gathered from Halchak et al. (2018); Henson (2018); de Rooij as well as the Aerospace Structural Metals Handbook (Gunderson et al., 2007), datasheets and other scientific literature. While there are obvious strong differences in the construction of rocket stages compared to satellites, many of the components and materials used in satellites are also used in rocket stages, like paint, MLI, batteries, wires, solder, PCBs, and CFRP. These components are modeled as for the satellites. The resulting mass composition as well as the relevant materials in use are given in Table 3. In the following, the different components and their typical materials are described, again giving the relative fraction of each material within its associated group and the source of the elemental mass composition in parenthesis when they are first mentioned. If no source is given, the composition is taken from Gunderson et al. (2007).

Propellant tanks, structure and payload adapters. They make up the largest mass portion by far. Aluminum alloys are favored due to their low weight (Henson, 2018). The workhorse alloy is 2219 (we assume 50%), but 2014 and newer aluminum lithium alloys like 2195 are used as well (each assumed 10% mass). Stainless steels are used to a lesser extent, for example in rare (because technically challenging) ballon tank designs such as 301 (AK Steel Corporation, 2007b) in the Centaur upper stage. But they appear also in standard tank designs such as 410 (AK Steel Corporation, 2007f) used in the Delta II upper stage (Steckel & Adams, 2018); we assume 5% each. For structure, aluminum alloys like 7075 as well as CFRP are used (Dumon et al., 2022; Beck et al., 2019; Toumi, 2019). We assume 10% mass portion for each.

Payload adapters normally are made from aluminum alloys such as 7075 as well as CFRP (e. g. Dumon et al., 2022); we assume an equal share of mass.

Rocket engines. Rocket engines comprise several components, namely a thrust chamber inner liner, thrust chamber jacket, nozzle and nozzle extension, feedlines and tubes, turbopumps, and valves. The mass fraction of each of these components differs depending on the engine cycle. We compute an average of the mass distribution of these components given in Tizón & Roman (2017) for the three different cycles. By multiplying these mass fractions with the average mass fraction of an engine in a rocket upper stage, one obtains the overall mass fraction of the specific engine components.

The thrust chamber wall (sometimes referred to as the inner liner) consists of alloys that have been specifically designed to handle the high loads and temperatures. These are specific copper and copper-chromium alloys like Narloy-Z and CRCop-84 (Halchak et al., 2018; Sutton & Biblarz, 2017; Ellis, 2005), or superalloys like CTX 1, 3 and 909 (Carpenter Technology Corporation, 1994, 1990, 1989), and nickel-chromium alloys such as X-750 (Special Metals Corporation, 2004b). We assume 20% mass fraction each for Narloy-Z, CRCop-84, CuCr3, the CTX alloy class and X-750.

For the thrust chamber jacket, which usually cools the inner thrust chamber walls by propellant running through its tubes, sometimes the same materials as for the inner liner are used (Sutton & Biblarz, 2017). But stainless steels and nickel-chromium alloys are also common materials Halchak et al. (2018). Based on the frequency of use reported in the relevant literature, we assume 40% mass fraction shared equally between 316 (AK Steel Corporation, 2007d), 347 (Metalcor GmbH, 2025a) and A286 (ATI, 2012) stainless steels, and 15% shared equally between Inconel 600 (Special Metals Corporation, 2008), X-750, Narloy-Z and CRCop-84, each.

Nozzles can consist of the same materials as thrust chamber inner liners or thrust chamber jackets, but different materials are also sometimes employed (Halchak et al., 2018), for example nickel-chromium alloys such as 718 (Carpenter Technology Corporation, 2009; Böhler Edelstahl GmbH, 2005), Ti6Al4V (SLM Solution Group Ag, 2019), and C-103 Niobium alloy (ATI, 2024). These are also used in rocket nozzle extensions which are needed for vacuum engine versions. Due to the generally lower temperatures compared to the nozzle close to the thrust chamber, carbon-fiber reinforced carbon (CFRC) is also a common option (Halchak et al., 2018; L3Harris Technologies, Inc., 2025). Based on the literature, we tentatively assume 25% CRFC, 20% C-103, and 20% shared equally between the three stainless steels (above) and 10% shared equally between 718, Inconel 600 and Ti6Al4V, each.

Feedlines and tubes are usually constructed from austenitic stainless steels, mainly 321 (AK Steel Corporation, 2007e), although 347 and A286 stainless steel, nickel-chromium 718 alloy, Hastelloy (de Rooij), aluminum alloys such as 6061 (thyssenkrupp Materials Services GmbH, 2018) and Ti6Al4V are also used (Halchak et al., 2018; Henson, 2018). Based on their frequency of use as reported in the relevant literature, we tentatively assume 30% 321 steel, 20% each for 347 and A286 steel, 10% each for 6061 and Ti6Al4V, and 5% each for 718 and Hastelloy.

Turbopumps employ a wide range of durable and temperature resistent materials (Halchak et al., 2018). Housing components are composed of nickel-chromium alloys 625 (Special Metals Corporation, 2006) and 718, stainless steels like A286 and Incoloy 903 (Special Metals Corporation, 2004a), and cobalt-based alloys like Haynes 188 (Haynes International, Inc., 2018). Pumping elements need extremely hard materials such as silicon nitride, Cronidur 30 (Energietechnik Essen GmbH) and 440C stainless steel (Carpenter Technology Corporation, 1987), or 9310 low-carbon steel (Service Steel Aerospace Corp.). While other alloys and steels are certainly in use, the materials classes will not be largely different due to the physical conditions the materials must endure. Therefore, we assume equal mass fractions of the 9 materials listed here to obtain a representative average turbopump composition.

According to Halchak et al. (2018), valves usually consist of an aluminum alloy housing (like A357 (Gravity Cast Pvt. Ltd.) and 7075 alloys (Alcoa Mill products)), with nickel and titanium based alloys (such as Inconel 625 and Ti5Al2.5Sn (Schumacher Titan)) used for high-strength needs. The valve internals favor specific steels such as 15-5PH steel (AK Steel Corporation, 2007a). We assume a 20% equal share of these 5 representative materials.

Pressurization tanks. These tanks are made for pressurizing the main fuel tanks when their pressure drops due to more and more fuel being burnt by the engine. Composite overwrapped pressure vessel (COPV) tanks are common (e. g. Dumon et al., 2022) as well as Ti6Al4V tanks (e. g. Lips et al., 2013; Steckel & Adams, 2018) to hold the pressurization gas (normally helium). COPV tanks commonly consist of a Ti6Al4V liner which is wrapped by a CFRP-epoxy layer (MT Aerospace). All in all, we asssume a mass composition of 50% each of CFRP-epoxy and Ti6Al4V.

Reaction control system (RCS). An RCS system is needed to control spacecraft attitude. It consists of propellant tanks, made of Ti6Al4V (MT Aerospace; Arianegroup, 2021; Steckel & Adams, 2018) and multiple small thrusters to allow direction changes. Thruster use a lot of different materials (Arianegroup; Nammo (U.K.) Limited; Halchak et al., 2018) like Haynes 25 (Haynes International, Inc., 2022), 304L (AK Steel Corporation, 2007c) and 4550 (Smiths Advanced Metals) steel, ethylene propylene diene monomer (EPDM) rubber (determined from Oliveira et al., 2010) as well as carbon and glass cloth ablators (calculated from SGL Technic LLC, 2025; Park Aerospace Corp., 2019; AZO Materials, 2025). We assume a small portion (5%) of ablator remains until reentry, 10% EPDM rubber and the other 85% mass an equal share of the alloys.

Guidance/Avionics. Typically, electronics boxes made of aluminum alloys such as 6061 are used to house the PCBs. Other components include (as in satellites) wires, lithium-ion batteries and solder. We tentatively assume 50% electronics box mass, 20% PCB and wire mass (each) as well as 5% of solder (as in satellites, about a quarter of the PCB mass) and 5% of battery mass. The latter are assumed with a lower relative mass compared to satellites as especially for LEO launches, upper stages reenter within only a few orbits, thus no large battery charge is needed.

Others. A significant mass fraction also goes into paint, insulation foam for cryogenic stages, and MLI. The compositions of these items are adopted from the ones calculated for satellites, where assuming only white paint (with zink oxide pigments) and PU foam as insulation foam.

2.2.3. Falcon 9/Heavy upper stage composition

The Falcon 9/Heavy upper stage is modeled separately as it contributes a large fraction of the overall mass influx, as shown in Section 2.1. Its Merlin 1D vacuum engine makes up 550 kg of the approx. 4.25 t dry mass of the stage (Wade, 2019; Barker et al., 2024). As there is no detailed information about the remaining mass distribution available, we renormalize all other components of the average upper stage, so that the total mass

Table 3. Estimated average composition of different kinds of rocket stages.

Component	Mass fraction estimates (%)				Source of mass fraction (upper stage)	Typical materials	Material sources
	Upper stage	Core stage	Falcon 9/Hvy. upper stage	Starship up. st.			
Rocket engine	**9.6**	**18.0**	**13.8**	**18.0**	Mean AVUM, Delta II		
Feedlines/Tubes	0.8	1.5	1.1	1.5	Tizón & Roman (2017)	321, 347, A286 stainless steel, Al 6061, Ti6Al4V, Inconel 718, Hastelloy	Henson (2018); Halchak et al. (2018); AK Steel Corporation (2007e); Metalcor GmbH (2025a); ATI (2012); thyssenkrupp Materials Services GmbH (2018); SLM Solution Group Ag (2019); Carpenter Technology Corporation (2009); Böhler Edelstahl GmbH (2005); de Rooij
Valves	0.9	1.6	1.2	1.6	Tizón & Roman (2017)	Al A357, 7075, Inconel 625, Ti5Al2.5Sn, 15-5 PH steel	Halchak et al. (2018); Gravity Cast Pvt. Ltd.; Alcoa Mill products; Special Metals Corporation (2006); Schumacher Titan; AK Steel Corporation (2007a)
Thrust chamber inner liner	2.1	3.9	3.0	3.9	Tizón & Roman (2017)	Narloy-Z, Cu-Cr alloy, CRCop-84, CTX 1, CTX 3, CTX 909, HPM X750	Halchak et al. (2018); Gunderson et al. (2007); Carpenter Technology Corporation (1994, 1990, 1989); Special Metals Corporation (2004b)
Turbopumps	2.7	5.2	3.9	5.1	Tizón & Roman (2017)	Silicon nitride, Inconel 625, A286, Incoloy 903, Haynes 188, Cronidur 30 stainless steel, 440C, E 9310, Inconel 718	Halchak et al. (2018); Special Metals Corporation (2006); ATI (2012); Special Metals Corporation (2004a); Haynes International, Inc. (2018); Energietechnik Essen GmbH; Carpenter Technology Corporation (1987); Service Steel Aerospace Corp.; Carpenter Technology Corporation (2009); Böhler Edelstahl GmbH (2005)
Thrust chamber jacket	0.4	0.8	0.6	0.8	Tizón & Roman (2017)	316, 347, A286, Inconel 600, HPM X750, Narloy-Z, CRCop-84	Halchak et al. (2018); AK Steel Corporation (2007d); Metalcor GmbH (2025a); ATI (2012); Special Metals Corporation (2008, 2004b); Gunderson et al. (2007)
Nozzle and nozzle extension	2.7	5.0	3.8	5.0	Tizón & Roman (2017)	C-103, 316, 347, A286, Inconel 718, Inconel 600, Ti6Al4V, CFRC, Cu-Cr alloy	Halchak et al. (2018); ATI (2024); AK Steel Corporation (2007d); Metalcor GmbH (2025a); ATI (2012); Carpenter Technology Corporation (2009); Böhler Edelstahl GmbH (2005); Special Metals Corporation (2008); SLM Solution Group Ag (2019); L3Harris Technologies, Inc. (2025)
Pressurization tanks	5.2	5.1	5.0	2.9	Mean AVUM, Delta II	Ti6Al4V, CFRP (epoxy-based)	MT Aerospace; SLM Solution Group Ag (2019); Sun et al. (2015); Metzler et al. (2016); Wen et al. (2024); Bonvoisin et al. (2023)
RCS system	**3.8**	**3.8**	**3.6**	**2.2**			
Monopropellant tanks	1.6	1.6	1.6	0.9	Mean AVUM, Delta II	Ti6Al4V	MT Aerospace; Arianegroup (2021); SLM Solution Group Ag (2019)
Monopropellant thrusters	2.2	2.1	2.1	1.2	Half of AVUM	Carbon cloth phenolic, glass cloth phenolic, Haynes 25, 304L, Radiometal 4550, EPDM rubber	Nammo (U.K.) Limited; Halchak et al. (2018); Haynes International, Inc. (2022); AK Steel Corporation (2007c); Smiths Advanced Metals; Oliveira et al. (2010); SGL Technic LLC (2025); Park Aerospace Corp. (2019); AZO Materials (2025)
Guidance/Avionics	**15.5**	**15.2**	**14.8**	**8.8**	Mean AVUM, Delta II		
Electronics boxes	7.7	7.6	7.4	4.4	Assumed 50%	Al 6061	thyssenkrupp Materials Services GmbH (2018)
Wires and cables	3.1	3.0	3.0	1.8	See satellite	See satellite	See satellite
PCBs	3.1	3.0	3.0	1.8	See satellite	See satellite	See satellite
Solder	0.8	0.8	0.7	0.4	See satellite	See satellite	See satellite
Li-ion batteries	0.8	0.8	0.7	0.4	See satellite	See satellite	See satellite
Payload adapter	7.0	-	6.7	-	Mean AVUM, Delta II	CFRP, AA 7075	Dumon et al. (2022)
Propellant tanks/Structure	51.5	50.6	49.1	60.0	Mean AVUM, Delta II, Toumi (2019)	AA 2219, AA 2014, AA 2195, 301, 410, CFRP, 7075, 2198 (Falcon upper stage), 304 (Starship)	Henson (2018); Steckel & Adams (2018); Dumon et al. (2022); Beck et al. (2019); Toumi (2019); Wanhill (2014); AK Steel Corporation (2007b,c,f); Gunderson et al. (2007); de Rooij
Paint	2.2	2.2	2.1	-	Toumi (2019), Beck et al. (2019)	Silicone + zinc oxide	Lecadre-Scotto et al. (2025); Kayhan et al. (2012)
Insulation foam	2.5	2.5	2.4	-	Toumi (2019), Beck et al. (2019)	Polyurethane	See satellite
MLI/Thermal protection	2.7	2.6	2.5	1.5	Toumi (2019), Beck et al. (2019)	See satellite	See satellite
Thermal protection system	-	-	-	6.7	Calculated (see text)	Silica fibres	Stiles (2003)
Total	100	100	100	100			

fraction is 100%. The Falcon 9/Heavy upper stage is known to use 2198 aluminum lithium alloy for its propellant tank walls, while the domes are made from standard aluminum alloy (we assume a share of 2219 and 2014) (Wanhill, 2014; Space Exploration Technologies Corp., 2025). We calculate the wall mass to be 68% of the whole propellant tank using dimension values from Wittal et al. (2022). As mentioned in an interview (Amy Svitak, 2011), the Merlin 1D engine employs a nickel cobalt inner liner (we assume the CTX alloy series, see above) and most probably a copper alloy jacket (Jonathan Goff, 2006), for example Narloy-Z or CRCop-84. The nozzle is reported to be made from C-103 niobium alloy.

2.2.4. *Starship upper stage composition*

Due to its enormous dry mass of around 120 t (see Section 2.1) the Starship upper stage composition is modeled separately. We calculate the mass of the 6 Raptor engines to make up about 18.0% of the overall mass, using reported engine dry mass by the manufacturer and assuming a 50% mass increase for the 3 vacuum version ones due to the nozzle extension. The enormous size of the rocket stage increases the relative mass of the propellant tank/structure, we estimate 60%. Starship employs a thermal protection system using ceramic tiles, most probably similar to the Space Shuttle's silica fibre tiles (Stiles, 2003). From information about the used tile numbers and dimensions (SpaceX, 2024), we infer about 6.7% of the mass belongs to the thermal protection system, which is reasonably close to estimates in Herberhold et al. (2025). All this reduces the relative mass of avionics, RCS constrol system, MLI and pressurization tanks compared to the average upper stage.

The Starship upper stage is constructed from stainless steel; it is highly likely that the composition is close to 304 stainless steel. Furthermore, no paint, insulation foam or payload adapter seems to be used. For all other components, we assume the same materials being used as in the average upper stage, as there is no further detailed information available about the composition of the Starship subsystems.

2.2.5. *Core stage composition*

While the relative mass of the engines are higher for core stages (Schulz & Glassmeier, 2021), the components used in both are the same (despite no payload adapter being used in the core stages). We adopt the engine mass of 18% from Schulz & Glassmeier (2021), and set the propellant tank and structure mass to 60% due to the larger overall stage size. All other components are renormalized.

2.3. *Ablation fraction*

The amount of material ablated from space waste upon atmospheric re-entry is highly dependent on re-entry parameters such as re-entry angle and velocity as well as object characteristics such as the ballistic coefficient. Additionally, different material parameters like melting and vaporization temperatures lead to differential ablation, where relatively volatile elements ablate much more rapidly than refractory species (Janches et al., 2009). This is known to strongly influence the relative injection of elements for the meteoric input. Furthermore, the differentiated nature of space waste leads to internal components being shielded from ablation. Both these aspects have been observed in wind tunnel experiments (Bonvoisin et al., 2023), as well as from recovered ground debris. There exist a plethora of tools to model the destructive re-entry of spacecraft, which take into account all of the mentioned aspects with varying levels of maturity. However, these so far have focused on ground-risk estimation, lack comprehensive validation against observations of atmospheric ablation, and considerable uncertainties apply (De Persis & Lemmens, 2024). Additionally, the lack of openly available detailed geometrical spacecraft models currently prevents the use of such models to determine average ablation fractions.

As there is currently no satisfactory data available to represent the complex nature of space waste ablation, we adopt constant ablation rates depending on the type of object from Schulz & Glassmeier (2021). Based on literature review, they find 80% ablated from satellites and debris, 65% ablated from all upper stages, and 30% from core stages. The remaining fractions are expected to impact ground. We do not assume the separate ablation fraction of 100% for large constellation satellites, because Ott & Bonnal (2025) point out that despite manufacturer claims of complete demise, constellation satellite remnants have been found on ground.

2.4. *Uncertainties*

The presented data are gathered from a wide range of sources, each with their own uncertainties. In the vast majority of cases, no uncertainties are provided. Furthermore, some values have to be assumed based on sensible approximations and extrapolations, because of the lack of data. This means that for most of the presented values, no uncertainty ranges are readily available. In order to get an impression of the resilience of the injection values, which are calculated from mass influx, composition and ablation fraction, we therefore estimate reasonable uncertainty ranges by comparison to other data or literature. In need of better data, we assume a normal distribution of the estimator for all used values, which allows the resulting uncertainty ranges to be quoted as 3σ-levels. Thus, Gaussian error propagation can be used to obtain a 3σ uncertainty for injection estimates.

2.4.1. *Mass influx uncertainty*

Although the database of McDowell (2025c) meticulously documents orbital reentries, dry masses of objects are partially estimated based on available information and can differ from values in other databases such as DISCOS (ESA, 2025) and others (e. g. see references in Barker et al., 2024). We estimate the uncertainty range by comparing the DISCOS and RCat annual influx estimates. It is important to note that the values from DISCOS are inflated due to satellite wet masses (masses including initial propellant) often being used instead of dry mass estimates. We determine the maximum deviation of both databases by calculating the maximum relative difference after normalizing the DISCOS values to the mean of the RCat data. That way, the wet mass bias is taken out of the equation. The maximum relative difference amounts to 3%, which we conservatively adopt as the uncertainty range. We also adopt this value for core stages.

2.4.2. *Elemental composition uncertainty*

While data from numerous different sources could be combined, there are also parts of the estimation where no data could be found and educated assumptions had to be made. We refrain from estimating uncertainties for all the different numbers gathered to come up with a combined, average elemental composition of satellites, different upper stages and core stages, but instead adopt a general uncertainty for different elements, depending on their maturity level. We introduce four different maturity levels: for elements which are abundant in many different material groups and components, and have well documented elemental compositions, we estimate a 3σ uncertainty equal to 40% of the elemental mass fraction. We also apply this to elements, which are known to be present in only one or a small number of components, but where we have reason to believe in a good estimate (e. g. due to data maturity). Elements H, Li, B, C, N, O, Mg, Al, Si, P, Ti, Cr, Mn, Fe, Ni, Cu, Zn, Mo, and Sn are categorized in this group.

For medium level maturity, we adopt a 3σ uncertainty of 80% of the elemental mass fraction. Here we group elements for which some credible information is available, but still the mass portion could differ more strongly. Such are Be, F, Na, S, Cl, K, Ca, V, Ga, Ge, As, Br, Zr, Nb, Ag, In, Ba, La, Ce, Hf, Ta, W and Pb.

For elements with absolute injection masses below 0.05 t, we only provide an upper limit because an unusually pronounced use of this specific element in only a few spacecraft would result in a large change of the actual injection value.

Lastly, elements where either there is little to no information, the elemental mass portion is 0 or very high uncertainties are expected, are disregarded. This group includes all the other elements and we do not consider those further.

2.4.3. *Ablation fraction uncertainty*

Ablation values are still uncertain due to a lack of dedicated in-flight experiments and observations. There exist no detailed measurements of survival portions which would allow statistical uncertainties to be evaluated, but estimated values come from findings of remnants of rocket bodies or satellites as well as modeling. The latter are not validated against measurements and thus the results have to be handled with caution. An overview study by Pardini & Anselmo (2025) assumes a range of 70 to 95% ablated mass fraction for orbital objects, while Ailor et al. (2005) work with 60 to 90%. Based on this, we conservatively estimate the 3σ-level of uncertainty at 15% for upper stages and satellites. For suborbital stages, the uncertainty is higher, as much fewer findings exist. We estimate 20%, generating a conservative range of 10 to 50% ablated mass fraction. These large uncertainty ranges also reflect the neglecting of the complex ablation behavior of space waste, such as the differential ablation of different elements.

2.4.4. *Uncertainty propagation*

The estimation of the 3σ uncertainties allows to use Gaussian error propagation to yield errors for the total injected mass per year as well as injected mass per year of specific elements. The total injected mass per year $\dot{m}_{\text{injection,total}}$ can be calculated by summing over the product of the mass influx $\dot{m}_{\text{influx},i}$ of each object type i (satellite, upper stage, or core stage) and the respective ablation fractions a_i:

$$\dot{m}_{\text{injection,total}} = \sum_i \dot{m}_{\text{influx},i}\, a_i. \tag{1}$$

The uncertainty can then be calculated via

$$\sigma_{\dot{m}_{\text{injection,total}}} = \sqrt{\sum_i a_i^2 \sigma^2_{\dot{m}_{\text{influx},i}} + \sum_i \dot{m}^2_{\text{influx},i}\, \sigma^2_{a_i}}. \tag{2}$$

with $\sigma_{\dot{m}_{\text{influx},j}} = 0.03\, \dot{m}_{\text{influx},j}$ and $a_i = 0.15$ for satellites and upper stages, and 0.2 for core stages (as explained above). The annually injected mass $\dot{m}_{\text{injection},E}$ of a specific chemical element E is

$$\dot{m}_{\text{injection},E} = \sum_j \dot{m}_{\text{influx},j}\, a_j\, c_{E,j}. \tag{3}$$

using the relative abundance of the element within each object group $c_{E,j}$. Here, upper stages have to be differentiated too, meaning j is a placeholder for the groups: satellites, Falcon 9/Heavy upper stages, Starship upper stages, all other upper stages, and core stages. The uncertainty then is determined via:

$$\sigma_{\dot{m}_{\text{injection},E}} = \sqrt{\sum_j a_j^2 c_{E,j}^2 \sigma^2_{\dot{m}_{\text{influx},j}} + \sum_j \dot{m}^2_{\text{influx},j} c_{E,j}^2 \sigma^2_{a_j} + \sum_j \dot{m}^2_{\text{influx},j} a_j^2 \sigma^2_{c_{E,j}}} \tag{4}$$

with $\sigma_{c_{E,j}} = p_E\, c_{E,j}$, where p_E is either 0.4 or 0.8, depending on the above discussed maturity level categorization of the specific element. Other derived uncertainties within this study have also been calculated using Gaussian error propagation.

3. Natural injection

We adapt the estimate of the annual meteoric mass influx to Earth's atmosphere by Schulz & Glassmeier (2021), who differentiated between dust particles and larger bolides. For the former, some elements in the composition were not estimated. We complement these by using the elemental abundances of CI-chondrites (Lodders et al., 2025), and renormalize to 100% mass. It should be noted that general ablation factors are taken into account, but not differential ablation, as in other studies, such as the one by Carrillo-Sánchez et al. (2020).

4. Results, comparisons and discussion

By combining the information about mass influx, composition and ablation efficiency we arrive at estimates of the mass annually injected into Earth's atmosphere by ablating space waste, either the total(using Eq. 1) or broken down to different elements (using Eq. 3). In order to put this injection into perspective, we compare to the estimated annual natural injection of matter from ablating meteoroids as well as measurements of elements in stratospheric aerosols.

4.1. Total influx and injection

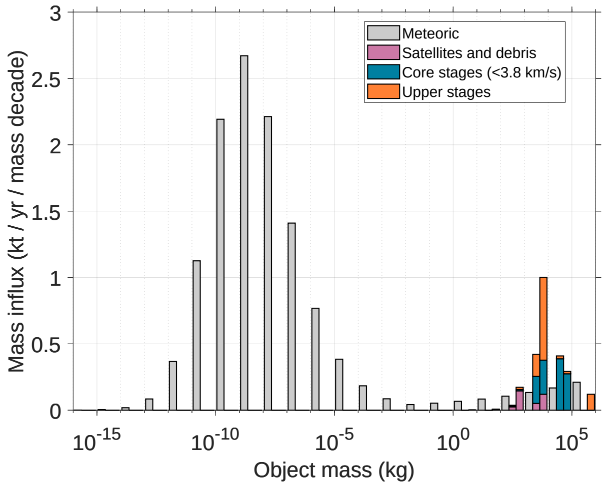

Fig. 2. Variation of the annual mass influx to the top of the atmosphere with object mass. The object mass is binned into mass decades. Three different mass influxes are shown: The gray bars depict the annual meteoric mass influx using values from (Schulz & Glassmeier, 2021), which is the mean model by Drolshagen et al. (2017). The middle bar shows the space waste mass influx in 2020, the right bar for 2024, both broken down by object type. Clearly, the space waste influx consists of large objects compared to the meteoric influx.

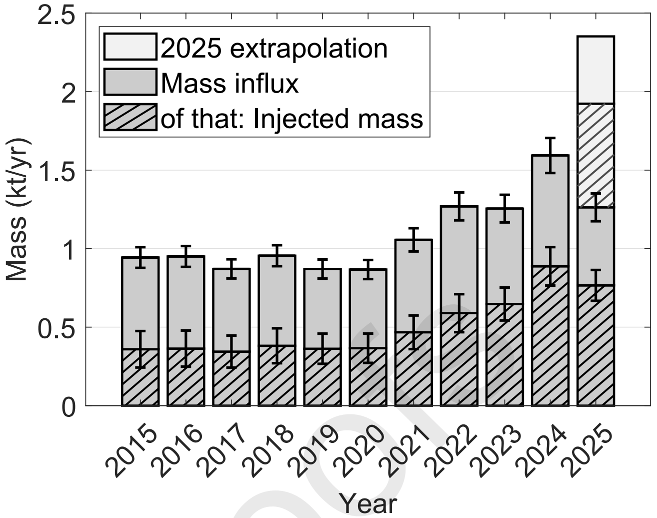

Fig. 3. Annual space waste mass influx to the top of the atmosphere and the fraction of that, which ablated was thus injected into the atmosphere (hatched area). For 2025, an extrapolation for the rest of the year (after July 15th 2025) is shown in the lighter gray, again with the hatched area representing the ablated mass. All mass not ablated reaches Earth's surface.

As shown in Figure 2, the space waste mass influx (colored bars showing years 2020 and 2024) to the top of the atmosphere is still considerably smaller than the annual meteoric influx (gray bars). Clearly, there has been as strong increase of space waste mass influx in only the past 4 years due to increased launch activity (especially because of large satellite constellations), that led to more upper stages reentering and also the onset of large constellation satellites reentering after their end of life. Clearly, space waste mass influx can be differentiated quite well by its size, satellites mostly being 0.1 to 10 t in mass, core stages 1–100 t, and upper stages mostly in the 1–10 t range. With the launch trials of Starship, from 2023 onward, objects with masses above 100 t have started to add to destructive reentry. These large masses are very different from the meteoric input. The latter dominates the mass influx with trillions of dust particles with masses of the order of μg.

The space waste mass influx to the top of the atmosphere, together with the fraction, that ablates and is thus injected into the atmosphere are plotted in Figure 3. The corresponding numbers are given in Table 1 for the mass influx and Table 4 for the injected mass (values in parenthesis are the percentage compared to the natural injection). While the mass influx has been close to 1 kt in the years 2015 to 2020 (see Table 1), the annual injected mass was only at 340 to 380 t/yr. In general, the injected mass makes up 40 to 60% of the mass influx, depending on the relative amount of satellites and the different rocket stages. The rest survives reentry and impacts the ground. From 2021 onward, an increase in mass influx as well as injected mass can be observed. In 2024, 887 ± 123 t of material was injected into the atmosphere. Extrapolating from the current data assuming a constant rate, for 2025 we expect around 1.4 kt, very close to the probable scenario (Scenario 1) of Schulz & Glassmeier (2021). In the maximum scenario (Scenario 2) of Schulz & Glassmeier (2021), an annual injected mass of 4.4 kt is to be expected, about a third of the annual naturally injected mass.

4.2. Injection by elements

While the total injected mass from space waste is an order of magnitude below the natural injection even during 2024 (7% compared to the natural injection), the relative comparison looking at the different elements groups reveals that it is double that value for metals (14%). This is due to the higher portion of metals in space waste and the considerably lower melting temperatures of metals compared with the metal silicates of which meteoroids are mostly composed. This is also the case for other years and both future scenarios, as shown in Table 4. Metalloids (B, Si, Ge, As, Sb and Te) are dominated by the natural input due to the high amount of silicon in meteoroids; this is also the case with non-metals, which are mostly organic elements highly abundant in meteoroids.

Table 5 shows the injected mass differentiated by elements. Uncertainties have been calculated by applying Gaussian error propagation on the uncertainty estimates of Section 2.4. A 3σ level of certainty is given to reflect an interval within which injection values are lying with very high probability. As uncertainties were not determined statistically but had to be estimated, it is possible that actual values can still lie outside this interval. The annual injection masses for an average of 2015 to 2020 and each year from 2021 up to 2024, as well as the two scenarios, are compared to the natural injection: values in yellow show injection masses surpassing the estimated annual meteoric input up to a factor of 2; orange depicts a factor of 2–5 times higher; and red at least 5 times the meteoric injected mass. Clearly, the abundant use of certain metal elements leads to a large number of them dominating the natural input. In 2015, 18 metal elements dominated the natural injection, while in 2024

Table 4. Injected mass (meaning post-ablation) by element group in t/yr. Percentages in parentheses are relative to the meteoric input. The uncertainty for the total injected mass is calculated according to Section 2.4. Errors in the last column represent 3σ uncertainties calculated using Eq. (2).
*until 16th of July 2025.
**extrapolated to end of 2025.

Year/ Scenario	Metals (t/yr)		Metalloids (t/yr)		Non-metals (t/yr)		Total (t/yr)		
2015	283	(6)	1	(<1)	75	(1)	359	± 116	(3)
2016	289	(7)	1	(<1)	74	(1)	364	± 115	(3)
2017	272	(6)	1	(<1)	71	(1)	344	± 102	(3)
2018	299	(7)	1	(<1)	81	(1)	382	± 111	(3)
2019	282	(6)	1	(<1)	79	(1)	363	± 96	(3)
2020	288	(7)	1	(<1)	76	(1)	366	± 93	(3)
2021	364	(8)	1	(<1)	102	(2)	467	± 107	(4)
2022	456	(10)	2	(<1)	131	(2)	589	± 121	(5)
2023	515	(12)	2	(<1)	130	(2)	647	± 105	(5)
2024	688	(16)	3	(<1)	196	(3)	887	± 123	(7)
*2025**	*611*	*(14)*	*4*	*(<1)*	*152*	*(2)*	*766*	*± 98*	*(6)*
*2025***							*1426*		*(12)*
Scen. 1	1025	(23)	6	(<1)	427	(7)	1458	± 239	(12)
Scen. 2	3079	(70)	19	(1)	1328	(22)	4426	± 696	(36)
Meteoritic	4369		1788		6167		12325		

this increased to 24 elements. In a 75,000 large constellation satellite scenario (Scenario 2), this number could increase to 30. The notable element with a high absolute anthropogenic input is Al, but also C, Fe, Cu, O, Ti, Ni, Cr and even Si and Nb. Of these, C, Fe, O and Si have a much larger natural input due to their high abundance in meteoroids; the anthropogenic injection is currently not relevant. Ni and Cr are only comparable to the meteoric injection for Scenario 2. The space waste injection of Al, Cu, Ti and Nb, however, has dominated the meteoric injection since at least 2015. In particular, the transition metals Cu, Ti and Nb are potentially capable of introducing new chemistry pathways in Earth's atmosphere, because these transition metals can have at least two accessible oxidation states and hence participate in catalytic cycles. While a number of the anthropogenically dominating elements have injection values below 10 t/yr — orders of magnitude lower than tropospheric emissions (see e. g. Zhu et al., 2020) — they are much less abundant in the meteoric input. Note that although the total mass input is low, the amounts are sufficient to be detected in the atmosphere and thus these elements can serve as tracers for space waste pollution of the atmosphere. Relevant elements are Li, B, F, V, Co, Zn, Ge, Br, Zr, Mo, Ag, Sn, Ba, Hf, Ta, W and Pb. While Be, In and Ce dominate over the natural influx as well, the general amount of these elements in meteoroids as well as anthropogenic materials is extremely low; the anthropogenic injection is estimated below 50 kg in 2024.

Comparison of the presented injection values with previous estimates for 2019 by Schulz & Glassmeier (2021) shows them strongly underestimating carbon and magnesium injection. Here, several organic-containing materials like adhesives, foams or CFRP have been considered; magnesium can be found in optical materials and several alloys not considered in the previous study. In contrast, Schulz & Glassmeier (2021) overestimated the use of germanium by an order of magnitude — this may be attributed to a substantial overestimation of the solar cell mass of a typical satellite. The previous estimates of Al, Si, Cr, Fe, and Cu are within the error ranges presented here, while titanium injection is estimated half and nickel injection double of the present estimate. This may be attributed to a much more detailed breakdown of used alloys in the present study. Overall, the present estimates constitute a substantial improvement over the previous estimates. In the following, specific elements will be addressed individually.

Lithium. Al-Li alloys and Li-ion batteries are the main contributors. Its abundance especially in rocket bodies might increase further in the coming years and decades, as Al-Li alloys are used more frequently. Lithium is especially interesting because it can be detected in the upper mesosphere above 80 km by lidar (Hauchecorne & Chanin, 1980; Jegou et al., 1980), and measurements were made well before space waste injection levels were significant, because neither Al-Li alloys nor Li-ion batteries being used in the space industry. Therefore, comparison to natural levels is possible using lidar, as done recently by Gerding et al. (2025); they already hypothesize space waste contribution. Another study (Wing et al., 2025) detected a lithium plume from a re-entering Falcon 9 upper stage via lidar.

Aluminum. Aluminum is the main element in space waste. Due to its light mass, it is the preferred structural material in the form of alloys. Therefore, it already dominates the meteoric injection since at least 2015. Due to its high mass input compared to other elements, it has been the focus of past studies (Schulz & Glassmeier, 2021; Shutler et al., 2022; Miraux et al., 2022; Jain, 2023; Barker et al., 2024; Ferreira et al., 2024). Possible effects on the atmosphere include changed radiative forcing from aerosol particles, but also direct and catalytic destruction of ozone on alumina (Al_2O_3) particle surfaces (Hanning-Lee et al., 1996; Molina et al., 1997). While the dominance

Table 5. Annual elemental mass injection (meaning post-ablation) estimates for the average of 2015–2020, the years 2021 to 2024 and the two future scenarios together with the annual meteoric injection in t/yr. Note that both the space waste and meteoric injection estimates are with general ablation factors applied, but without any differential ablation considered. For the meteoric injection, other studies such as by Carrillo-Sánchez et al. (2020) consider differential ablation. Space waste estimates 100–200% of the meteoric flux are marked yellow, ≥200% orange, and ≥500% red. The uncertainty is the 3σ estimate calculated using Eq. (4).

El.	Mean 2015–2020 (t/yr)	2021 (t/yr)	2022 (t/yr)	2023 (t/yr)	2024 (t/yr)	Scen. 1 (t/yr)	Scen. 2 (t/yr)	Meteoric (t/yr)
H	3.0 ± 1.1	4.0 ± 1.2	5.2 ± 1.5	5.1 ± 1.3	7.8 ± 2.0	16.6 ± 5.7	51.7 ± 18.2	221
Li	0.5 ± 0.2	0.7 ± 0.2	1.0 ± 0.3	1.1 ± 0.3	1.7 ± 0.5	2.7 ± 1.0	8.4 ± 3.2	0.02
Be	< 0.05	< 0.05	< 0.05	< 0.05	< 0.05	< 0.05	0.2 ± 0.1	3×10^{-4}
B	0.1 ± 0.0	0.2 ± 0.1	0.2 ± 0.1	0.2 ± 0.1	0.4 ± 0.1	1.0 ± 0.4	3.1 ± 1.2	0.009
C	51.2 ± 19.8	67.9 ± 21.9	86.7 ± 26.1	84.5 ± 22.0	127.0 ± 32.4	276.5 ± 94.2	857.0 ± 297.8	1154
N	2.8 ± 1.2	3.6 ± 1.3	4.6 ± 1.5	4.6 ± 1.2	6.6 ± 1.6	12.2 ± 4.0	37.1 ± 12.4	23
O	15.8 ± 5.7	21.4 ± 6.5	27.9 ± 8.0	30.1 ± 7.1	44.9 ± 11.0	94.4 ± 33.3	294.9 ± 106.1	4169
F	2.5 ± 1.4	3.4 ± 1.9	4.7 ± 2.7	4.4 ± 2.3	7.5 ± 4.4	21.1 ± 15.6	67.2 ± 50.4	1
Na	< 0.05	0.1 ± 0.0	0.1 ± 0.1	0.1 ± 0.1	0.2 ± 0.1	0.5 ± 0.4	1.6 ± 1.3	64
Mg	1.7 ± 0.6	2.3 ± 0.7	3.1 ± 0.9	2.9 ± 0.8	4.7 ± 1.3	11.5 ± 4.3	36.3 ± 13.8	1404
Al	175.7 ± 83.6	226.5 ± 86.8	285.4 ± 99.4	287.1 ± 85.4	397.0 ± 106.1	618.6 ± 212.8	1855.5 ± 631.4	142
Si	6.2 ± 2.4	8.1 ± 2.7	10.5 ± 3.2	13.1 ± 3.1	18.2 ± 4.2	32.3 ± 11.1	100.1 ± 35.0	1788
P	0.3 ± 0.1	0.5 ± 0.1	0.6 ± 0.2	0.6 ± 0.2	1.0 ± 0.3	3.0 ± 1.2	9.6 ± 3.9	23
S	< 0.05	< 0.05	0.1 ± 0.0	0.1 ± 0.0	0.1 ± 0.0	0.2 ± 0.1	0.5 ± 0.3	559
Cl	0.1 ± 0.1	0.2 ± 0.1	0.2 ± 0.1	0.2 ± 0.1	0.3 ± 0.1	0.7 ± 0.4	2.2 ± 1.4	15
K	< 0.05	0.1 ± 0.0	0.1 ± 0.1	0.1 ± 0.1	0.1 ± 0.1	0.5 ± 0.4	1.5 ± 1.2	8
Ca	0.4 ± 0.2	0.5 ± 0.2	0.7 ± 0.3	0.7 ± 0.3	1.0 ± 0.4	2.1 ± 1.3	6.5 ± 4.2	94
Ti	14.2 ± 6.1	18.7 ± 6.5	23.7 ± 7.5	25.6 ± 6.6	35.8 ± 8.6	60.2 ± 19.8	183.5 ± 60.7	8
V	0.6 ± 0.4	0.8 ± 0.4	1.1 ± 0.5	1.1 ± 0.5	1.5 ± 0.6	2.5 ± 1.3	7.4 ± 4.1	1
Cr	7.5 ± 4.4	8.8 ± 4.4	10.2 ± 4.8	19.4 ± 6.0	21.9 ± 6.2	20.5 ± 9.0	59.4 ± 25.6	40
Mn	0.8 ± 0.4	1.0 ± 0.4	1.3 ± 0.5	1.7 ± 0.5	2.2 ± 0.5	2.5 ± 0.9	7.3 ± 2.7	23
Fe	28.4 ± 16.1	33.9 ± 16.2	40.0 ± 18.0	72.3 ± 21.6	83.2 ± 22.6	82.4 ± 34.1	240.8 ± 97.3	2477
Co	2.8 ± 1.7	3.6 ± 1.9	4.7 ± 2.3	5.2 ± 2.2	7.3 ± 3.0	11.3 ± 6.4	34.4 ± 20.0	5
Ni	11.8 ± 6.7	14.2 ± 6.7	17.2 ± 7.5	24.0 ± 6.9	29.0 ± 7.5	33.8 ± 14.2	99.2 ± 40.7	96
Cu	23.7 ± 11.3	29.8 ± 11.6	37.0 ± 13.2	37.6 ± 10.7	52.1 ± 13.3	97.7 ± 33.3	297.2 ± 101.2	2
Zn	3.1 ± 1.3	4.1 ± 1.4	5.2 ± 1.6	5.1 ± 1.4	7.3 ± 1.9	13.7 ± 4.5	41.9 ± 13.7	5
Ga	< 0.05	< 0.05	< 0.05	< 0.05	< 0.05	0.1 ± 0.1	0.4 ± 0.3	0.2
Ge	0.3 ± 0.2	0.4 ± 0.4	0.6 ± 0.5	0.5 ± 0.4	1.0 ± 0.9	3.8 ± 3.1	12.3 ± 10.1	0.5
As	< 0.05	< 0.05	< 0.05	< 0.05	< 0.05	0.1 ± 0.1	0.3 ± 0.2	0.2
Br	0.4 ± 0.2	0.6 ± 0.3	0.7 ± 0.3	0.8 ± 0.3	1.1 ± 0.5	2.2 ± 1.4	6.8 ± 4.3	1
Zr	0.2 ± 0.1	0.2 ± 0.1	0.3 ± 0.2	0.3 ± 0.2	0.4 ± 0.2	0.6 ± 0.3	1.8 ± 1.0	0.2
Nb	3.4 ± 2.4	4.8 ± 2.8	6.7 ± 3.9	8.9 ± 5.1	11.5 ± 6.9	5.7 ± 4.7	16.1 ± 13.1	0.004
Mo	0.5 ± 0.3	0.6 ± 0.3	0.7 ± 0.4	0.8 ± 0.3	1.0 ± 0.3	1.3 ± 0.7	3.8 ± 1.9	0.01
Ag	0.7 ± 0.5	1.0 ± 0.6	1.5 ± 0.9	1.4 ± 0.8	2.4 ± 1.5	6.9 ± 5.3	22.2 ± 17.2	0.003
In	< 0.05	< 0.05	< 0.05	< 0.05	< 0.05	< 0.05	0.1 ± 0.1	9×10^{-4}
Sn	1.8 ± 0.7	2.5 ± 0.8	3.2 ± 0.9	3.4 ± 0.8	5.0 ± 1.2	9.7 ± 3.3	30.2 ± 10.5	0.02
Ba	0.1 ± 0.1	0.1 ± 0.1	0.2 ± 0.1	0.2 ± 0.1	0.3 ± 0.2	0.8 ± 0.6	2.4 ± 1.8	0.04
La	< 0.05	< 0.05	< 0.05	< 0.05	< 0.05	< 0.05	< 0.05	0.003
Ce	< 0.05	< 0.05	< 0.05	< 0.05	< 0.05	0.1 ± 0.1	0.3 ± 0.3	0.009
Hf	0.3 ± 0.2	0.5 ± 0.3	0.7 ± 0.4	0.9 ± 0.5	1.2 ± 0.7	0.5 ± 0.4	1.5 ± 1.2	0.002
Ta	< 0.05	0.1 ± 0.0	0.1 ± 0.0	0.1 ± 0.0	0.1 ± 0.1	0.2 ± 0.1	0.6 ± 0.3	2×10^{-4}
W	0.5 ± 0.4	0.6 ± 0.4	0.7 ± 0.4	0.9 ± 0.4	1.1 ± 0.5	1.1 ± 0.8	3.0 ± 2.1	0.001
Pb	1.2 ± 0.6	1.6 ± 0.8	2.1 ± 1.0	2.2 ± 0.9	3.2 ± 1.4	6.1 ± 3.7	19.0 ± 11.8	0.03

of alumina from space waste ablation is proposed by equilibrium chemistry modeling post-ablation (Park et al., 2021), it is questionable whether this is oversimplified. Meteoroid ablation and atmospheric chemistry modeling suggest AlOH and $Al(OH)_2$ as the dominating chemical species at altitudes below 80 km (Plane et al., 2021), which is supported by the preliminary analysis of lab ablation experiments (Gomez Martin et al., 2025). The hydroxide species in particular suggest completely different pathways of influencing ozone levels as well as other atmospheric effects, yet to be determined.

Fluorine. Fluorine is present in rubbers and plastics, but especially in the electrolyte of lithium ion batteries as lithium hexafluorophosphate ($LiPF_6$). It has been detected often in stratospheric aerosol particles with space waste metals (Murphy et al., 2023), and its dominance over the meteoric input raises questions about possible atmospheric chemistry. A possible pathway could be the synthesis of hydrogen fluoride. However, the injected amount of fluorine is very low compared to the amount of fluorine (the majority from CFCs) already in the atmosphere (Raymond et al., 2025) — about 1 ppb translates to roughly 10^6 t in the stratosphere, a factor of 10^5 more than the space waste injection in 2024. For the mesosphere, due to its lower mass, this ratio drops to 500. In the thermosphere, the total fluorine is comparable to the total injection today. However, most of space waste is ablated below the thermosphere and is subsequently transported downwards.

Chlorine and bromine. The only sources of chlorine determined in this study include remnants in epoxy resins which are used in CFRP and as adhesives, coatings, etc. We did not find that they are usually part of the newer cyanate ester resins, contrary to Toumi (2019). Standard plastics like polychlorotrifluoroethylene (PCTFE) or polyvinyl chloride (PVC) naturally have chlorine in them, but seem to not be used regularly in space applications due to strong outgassing (de Rooij). As a result, the total chlorine injection by space waste is far lower than the meteoric input, even in extreme scenarios. This points towards the direct impact on for example ozone levels being too small to be measurable.

Bromine on the other hand, being present in PCBs, began to dominate over the naturally injected bromine in 2024 and might exceed the natural injection by a factor of 5 in the future. However, assuming a residence time of 5 years, the mass input of less than 5 t is very low compared to the bromine currently present in different atmospheric layers. Using a bromine concentration of 20 ppt (Wales et al., 2021) we arrive at a total bromine mass of about 15 kt in the stratosphere.

Arsenic. Contrary to presentations of preliminary results (Schulz et al., 2024, 2025) which were based on an inflated estimate of arsenic content in solar cell material (Toumi, 2019), the arsenic injection does not dominate over the natural injection. The compositional refinement using data sheets, and the literature of triple-junction solar cell materials, indicates that only a small amount of arsenic is being used. Thus, only in the extreme scenario do space waste injection levels dominate over the natural input from meteoroids. Compared to the annual tropospheric release of about 31 kt per year (Walsh et al., 1979), the anthropogenic atmospheric injection of less than 50 kg/yr is negligible when it comes to toxicity concerns.

Transition metals. Transition metals are known for their catalytic activity, for example as organic derivative or hydrate and oxide catalysts. The domination over the natural input of Ti, Co, Cu, Zn, Zr, Nb, Mo, Ag, Hf, Ta, W shows the need for a better understanding of the chemical pathways of these metals, especially with regards to cloud nucleation and stratospheric heterogeneous chemistry.

4.3. Comparison to stratospheric data

Due to atmospheric circulation, material from the mesosphere injection altitudes is transported towards the winter pole, where it descends within the polar vortex to the lower stratosphere. Murphy et al. (2023) analyzed individual stratospheric aerosol particles, calculating metal ratios relative to aluminum for the material coming from space waste reentry, excluding the meteoric injection. Thus, we can directly compare the elemental injection rates presented here to their findings. We use the data from 2022 to coincide with their measurements at the beginning of 2023. The comparison is shown in Table 6. For all elements, we see excellent agreement; values are well within the limits of uncertainty and the relative difference compared to the measured data is at 0%, 8%, and 22% for lithium, copper, and lead, respectively. This strongly support the findings by Murphy et al. (2023) of space waste remnants being present in stratospheric aerosol particles. By reducing the uncertainties of both methods, insights about possible differential ablation of spacecraft components and about different elements can be gained.

Table 6. Element injection (meaning post-ablation) relative to aluminum injection in 2022 for selected elements and the comparison values from Murphy et al. (2023). Values are given in %. Errors represent 3σ uncertainties.

Element	Relative ratio to Al (this study)		Relative ratio to Al (Murphy et al. 2023)	
Li	0.4	± 0.2	0.4	± 0.2
Be	0.003	± 0.003		
Ti	8.3	± 3.9		
Cr	3.6	± 2.1		
Cu	13	± 7	12	± 6
Nb	2.3	± 1.6		
Mo	0.3	± 0.2		
Ag	0.5	± 0.4		
Sn	1.1	± 0.5		
Hf	0.2	± 0.2		
Ta	0.03	± 0.02		
W	0.3	± 0.2		
Pb	0.7	± 0.4	0.9	± 0.5

Comparisons to meteoric injection were presented by Murphy et al. (2023) as well. They found more than 70% of the cumulative aluminum in particles strongly contaminated with space waste elements, and more than 90% for Li, Cu and Pb. For 2022, our results indicate that the fraction of space waste aluminum in the total injection from all natural and man-made materials is 67%, 98% for Li, 94% for Cu, and 99% for Pb. This excellent agreement points towards a high percentage of space waste ablated material being vaporized (as hypothesized by Murphy et al., 2023), instead of ablating as molten droplets and ending up in large particulates. Particles of sizes above (> 10μm) sediment to the ground within weeks and would not be detectable in the stratosphere (Glassmeier & Schulz, 2025). On the other hand, particles of sizes between 10 and 100 nm are transported from mesospheric injection altitudes to the stratosphere by the residual circulation and can reside there for a few years and thus accumulate (Maloney et al., 2025). By better constraining the uncertainties in both the present study and Murphy et al. (2023), and better understanding stratospheric particle accumulation, one could possibly work to get closer to a size distribution of space waste ablation emissions. Due to the different residence times in the atmosphere and different total surface area, particle size distributions are a key element in determining the importance of ablated space waste in the middle atmosphere.

The elements suspected of being space waste remnants in

Murphy et al. (2023) are also predicted in our study, namely Li, Al, Cu, Nb, Ag, Hf, Pb, Be, Mg, Ti, Cr, Fe, Ni, Zr, Ga, Mo, In, Sn, Ba, Ce, Ta and W. Elements not present in significant amounts here, but detected in their study are Sb and Bi, but also the rarely seen Cd, Pr and Nd. A further refinement of the compositional estimate should also focus on these.

5. Conclusion and outlook

These updated estimates of the annual influx and injection of space waste matter into Earth's atmosphere from 2015 up to 2025 confirm the anticipated strong increase in mass influx (e. g. Schulz & Glassmeier, 2021). Between 2020 and 2024, the injected mass has more than doubled, whereas it stayed almost constant in the years before, as did the mass influx. This shows that the onset of the large satellite constellation age is the driving factor of the increased space waste reentry into the atmosphere. The future scenarios adopted from Schulz & Glassmeier (2021) are slowly becoming reality with the mass injection extrapolated to the end of 2025 equaling future scenario 1.

Although the annually injected mass is still an order of magnitude smaller than that injected by meteoroids, the high abundance of metals in space waste results in a much higher ratio compared to the natural injection (17% in 2024). In a scenario of 75,000 large constellation satellites — which is well within reach of the current proposals and activities — this value could rise to 70% in the future. This percentage is lower than the original estimate in Schulz & Glassmeier (2021) due to an adjustment of the natural input and a much more detailed compositional evaluation of space waste. More importantly, a large number of elements — mainly metals — already dominate the natural injection. The number has increased from 18 elements in the 2015 to 24 in 2024, and could further increase to 30 in the future. They are mainly elements with low to medium natural injection levels. The element with the highest mass input by far is aluminum, which is regularly considered in studies. However, other dominating elements should also be considered, even if the injected mass is low. Notable elements include Cu, Ti, Nb, Co, Zn, Sn, Pb, Ag, Li, V, Hf, W, Ge, Mo, Zr, B, and Ba.

The wide variety of elements injected by re-entering space waste, combined with their dominance over the meteoric injection, underscores the need for comprehensive research on associated atmospheric effects. The fact that the presented injection estimates fit very well to measurements of stratospheric aerosol particles suggests that either a large portion of the injected material is vaporized during ablation or that a substantial amount of the injected material stays in the upper atmosphere for prolonged periods of time. The considerable injection of transition metals, which are known for their catalytic activity, raises question about long-term effects on Earth's atmosphere via yet unknown chemical pathways. This adds to existing worries about effects on ozone chemistry in the stratosphere (Schulz & Glassmeier, 2021; Shutler et al., 2022; Barker et al., 2024; Ferreira et al., 2024), increased cloud nucleation, or climate effects.

The present study considerably improved compared to the original estimates by Schulz & Glassmeier (2021). The consideration of various databases, industry input, material information, and literature allows for the computation of injection values for 43 elements, compared to 10 previously. Values for all other naturally occurring elements were obtained (up to atomic numbers of uranium excluding Tc, At, Fr, Pm and all noble gases) but not considered due to excessive uncertainties. In general, considerable uncertainties are still involved in all parts of the estimation, namely mass influx, space waste composition, and ablation behavior. In order to improve the estimates in the future, more detailed data is needed, especially from companies involved in supplying components and materials, and building and operating satellites and launchers. Precise data is needed on component materials, component mass fractions, dry masses of rocket stages and the trajectories of launchers. Additionally, much more research has to go into destructive ablation. Probably the largest source of uncertainty in this study is the oversimplification of the process of ablation. The neglecting of differential ablation of different elements and of re-entry and object parameters on ablation leads to considerable uncertainties. Thus, there is a need for dedicated searches for space waste that survived reentry and impacted ground, detailed observations of space waste ablation, and further ground experiments representative of the conditions of atmosphere re-entry. With future improvements concerning model uncertainty and especially validation with atmospheric ablation data, destructive re-entry models will be a candidate to largely improve the assumptions of ablation made in this study and thus improve the presented injection estimates.

Today's large satellite constellations amplify the problem of on-orbit space debris as well as the ground risk from impacts. Beside these well-discussed problems, the injection estimates presented here indicate a substantial risk associated with space waste re-entry and possible effects on Earth's atmosphere and thus the human habitat.

Acknowledgments

The authors want to thank James Beck, Andreas Hördt, Dennis Michael Jöckel, Viktoria Kutnohorsky, Tobias Lips, Martin Ross, and Martin Spel for stimulating discussion and helpful advice.

For our research we are using information from ESA DISCOS (Database and Information System Characterising Objects in Space), a single-source reference for launch information, object registration details, launch vehicle descriptions, as well as spacecraft information for all trackable, unclassified objects. We acknowledge ESA's efforts to maintain and operate this database with its APIs.

Appendix A: Rocket stages dry mass and re-entry velocity

Table 7 gives all rocket stages with their dry mass and re-entry velocity of orbital rockets active between 2015 and 2025. From that, for reach rocket, the total mass of the core stages (suborbital) which destructively re-enter the atmosphere (with velocities larger than 3.8 km/s, but not reaching orbital speed) can be derived, given in the last column of Table 7. Upper stages reaching orbit do not add to this total mass. Booster stages (stage number 0) are assumed to have speeds below 3.8 km/s; so are payload fairings (except for the Long March 4B and 4C). We also disregard all stages that make a controlled landing. Rockets that were launched, but failed to reach orbit (OS-M1, RS-1, Spectrum, Super Strypi (SPARK), Terran-1) as well as suborbital rockets are not considered. Stage mass data were obtained from Schulz & Glassmeier (2021), the German Aerospace Center (DLR), Barker et al. (2024), McDowell (2025b), and Krebs (2025). Velocity data were obtained from Schulz & Glassmeier (2021), the German Aerospace Center (DLR), Bautze-Scherff (2022), and calculated using trajectory data from launch videos. For some rockets, no information is available. In these cases, values were assumed (marked yellow in the Table) based on similar launch vehicles.

Appendix B: Satellite and rocket body average elemental composition

Table 8 gives the average elemental mass composition estimates for different types of space waste, namely satellites, the three different rocket upper stages, and rocket core stages. The compositions are calculated by first calculating the product of each material group/component mass fraction estimate (both are provided in Tables 2 for satellites and 3 for the four different rocket body types) with the fractions of the respective representative materials within each group (as mentioned in Section 2.2 and also for the average satellite in Table 9), and its elemental mass composition. The obtained elemental mass composition contributions are then summed over all materials, yielding the average elemental mass compositions. The color code of the elements in Table 8 describes the level of uncertainty introduced in Section 2.4.

Appendix C: Mass fractions of typical materials the modeled average LEO satellite.

Table 9 gives the modeled mass fractions of each material group (as given in Table 2) as well as the relative fraction of the modeled, typical materials within each material group. By calculating the product of the mass fraction of each material group, the relative fraction of the typical material within that group, and its elemental mass composition the elemental contribution to the average mass composition of a satellite can be determined. By summing the mass contribution of all the typical materials, the average satellite elemental mass composition, given in column 2 of Table 8, is obtained.

References

Haynes International, Inc. (2018). *Haynes 188*. Haynes International, Inc.

Haynes International, Inc. (2022). *Haynes 25*. Haynes International, Inc.

Space Exploration Technologies Corp. (2025). *Falcon user's guide*. Space Exploration Technologies Corp.

3M (2008). *MATERIAL SAFETY DATA SHEET Scotch-Weld(TM) Epoxy Adhesive 2216 B/A, Gray*. 3M St. Paul, Minnesota, USA.

Ailor, W., Hallman, W., Steckel, G. et al. (2005). Analysis of reentered debris and implications for survivability modeling. In D. Danesy (Ed.), *4th European Conference on Space Debris* (p. 539). volume 4 of *ESA Special Publication*.

AK Steel Corporation (2007a). *Product data sheet 15-5 PH stainless steel*. AK Steel Corporation West Chester, Ohio, USA.

AK Steel Corporation (2007b). *Product data sheet 301 stainless steel*. AK Steel Corporation West Chester, Ohio, USA.

AK Steel Corporation (2007c). *Product data sheet 304/304L stainless steel*. AK Steel Corporation West Chester, Ohio, USA.

AK Steel Corporation (2007d). *Product data sheet 316/316L stainless steel*. AK Steel Corporation West Chester, Ohio, USA.

AK Steel Corporation (2007e). *Product data sheet 321 stainless steel*. AK Steel Corporation West Chester, Ohio, USA.

AK Steel Corporation (2007f). *Product data sheet 410 stainless steel*. AK Steel Corporation West Chester, Ohio, USA.

Alcoa Mill products (). *ALLOY 7075 PLATE AND SHEET*. Alcoa Mill products Bettendorf, Iowa, USA.

Amy Svitak (2011). Profile: Elon musk, chief executive and chief technology officer of space exploration technologies. `https://spacenews.com/elon-musk-chief-executive-and-chief-technology-officer-space-explo` [Accessed 03-08-2025].

Arianegroup (). *1N, 20N, 400N nad hertiage thruster*. Arianegroup Taufkirchen, Germany.

Arianegroup (2021). *Propellant tanks*. Arianegroup Lampoldshausen, Germany.

ATI (2012). *Technical Data Sheet ATI A286*. ATI Pittsburgh, Pennsylvania, USA.

ATI (2024). *Technical Data Sheet ATI C103 Spherical Powder* . ATI.

AZO Materials (2025). E-Glass Fibre. `https://www.azom.com/article.aspx?ArticleID=764`. [Accessed 03-08-2025].

AZUR SPACE Solar Power GmbH (2016a). *30% Triple Junction GaAs Solar Cell — Type: TJ Solar Cell 3G30C - Advanced*. AZUR SPACE Solar Power GmbH Heilbronn, Germany.

AZUR SPACE Solar Power GmbH (2016b). *30% Triple Junction GaAs Solar Cell — Type: TJ Solar Cell 3G30C - Advanced (80µm)*. AZUR SPACE Solar Power GmbH Heilbronn, Germany.

AZUR SPACE Solar Power GmbH (2016c). *Silicon Solar Space Cell S 32 — Type: S 32*. AZUR SPACE Solar Power GmbH Heilbronn, Germany.

Barber, L. A. (2001). Copolymers of vinylidene flouride and hexaflouropropylene and process for preparing the same.

Barker, C. R., Marais, E. A., & McDowell, J. C. (2024). Global 3d rocket launch and re-entry air pollutant and co2 emissions at the onset of the megaconstellation era. *Scientific Data*, *11*(1), 1079. doi:`10.1038/s41597-024-03910-z`.

Bautze-Scherff, T. (2022). Preliminary launch trajectory simulation for artemis i with the space launch system.

Beck, J., Merrifield, J., Spel, M. et al. (2019). Aerothermodynamic assessment of atmospheric emissions from re-entry demise. In *ESA International Conference on Flight Vehicles, Aerothermodynamics and Re-entry Missions Engineering (FAR)*.

Bianchi, S. (2019). *ATMOSPHERIC IMPACT OF SPACECRAFT DEMISE D3: Final Report*. Technical Report TASI-SD-ARA-ORP-0106 ThalesAlenia Space.

Boley, A. C., & Byers, M. (2021). Satellite mega-constellations create risks in low earth orbit, the atmosphere and on earth. *Scientific Reports*, *11*(1), 10642. doi:`10.1038/s41598-021-89909-7`.

Bonvoisin, B., Meisnar, M., Merrifield, J. et al. (2023). Demisability assessment of space materials. *CEAS Space Journal*, *15*(1), 213–235. doi:`10.1007/s12567-022-00429-0`.

Borthomieu, Y. (2014). 14 - satellite lithium-ion batteries. In G. Pistoia (Ed.), *Lithium-Ion Batteries* (pp. 311–344). Amsterdam: Elsevier. doi:`https://doi.org/10.1016/B978-0-444-59513-3.00014-5`.

Borthomieu, Y., Armel, V., Guern, B. L. et al. (2019). VES16 Batteries for LEO and GEO Satellites. In *2019 Space Power Workshop*.

Böhler Edelstahl GmbH (2005). *L718*. Böhler Edelstahl GmbH Kapfenberg, Austria.

Carpenter Technology Corporation (1987). *Carpenter Stainless Type 440C*. Carpenter Technology Corporation.

Table 7. Rocket stage masses and re-entry velocities of rockets. The total mass of all suborbital stages of a rocket that destructively re-enter at speeds larger than 3.8 km/s is given in the last column. Assumed values are marked yellow. Certain rockets have different configurations, where the booster stage or the orbital stage differ in dry mass. In this case, the rockets are summarized and a green field depicts possible different configurations. When no data is available and no assumptions were made, the field is marked red.

Rocket	Stage dry mass (kg)					Stage re-entry velocity at 100 km (km/s)				Total re-entry mass with v>3.8 km/s (kg)
Stage #	0	1	2	3	4	1	2	3	4	
Angara 1.2	0	10150	2355	1000		<3.8	>3.8	orbital		2355
Angara (A5, A5 Orion, and A5 Persei)	39200	11000	4000	🟩		5.0	7.6	orbital		15000
Antares 230	0	19700	1392			3.8	orbital			19700
Ariane 5 (ECA and ES)	31000	14700	🟩			6.9	orbital			14700
Ariane 62	22000	14700	3000			4.5	orbital			14700
Astra Rocket 3	0	950	250			<3.8	orbital			0
Atlas V 4XY	🟩	21054	🟩			4.9	orbital			21054
Atlas V 5XY	🟩	21351	2030			4.9	orbital			21351
Atlas V N22	10200	22825	2030			4.9	orbital			22825
Ceres-1	0	590	274	86	2	<3.8	<3.8	>3.8	orbital	86
Chollima-1	0	🟥	500	🟥		<3.8	>3.8	orbital		500
Delta 4H	54400	27200	3420			6.0	orbital			27200
Delta 4M+ ((4,2), (5,2), and (5,4))	🟩	27200	🟩			4.9	orbital			27200
Delta II (types 7320, 7420, 7920)	🟩	5680	950			>3.8	orbital			5680
Dnepr	0	15000	3000	900		<3.8	>3.8	orbital		3000
Electron and Electron Curie	0	950	250	40		<3.8	7.6	orbital		250
Epsilon-2	0	8700	2000	800		2.1	5.7	orbital		2000
Epsilon-2 CLPS	0	8700	2000	800	155	2.1	5.7	> 5.7	orbital	2800
Falcon 9 (v1.1 and v1.2)	0	21100	3700			lands	orbital			0
Falcon Heavy	39500	21300	4250			lands	orbital			0
Firefly Alpha	0	2895	909			2.9	orbital			0
GSLV Mk II	24000	30000	4800	2200		4.8	orbital			30000
GSLV Mk III	62300	10100	4850			4.6	orbital			10100
GYUB - TV2	0	🟥	500	🟥		<3.8	>3.8	orbital		500
Gravity-1	🟥	🟥	2000	🟥		<3.8	>3.8	orbital		2000
H-IIA (202 and 204)	🟩	12900	3100			5.1	orbital			12900
H-IIB	42200	24200	3400			5.5	orbital			24200
H-III 22	🟥	25000	🟥			3.6	orbital			0
Jielong-1	0	🟥	🟥			<3.8	orbital			0
Jielong-3	0	8700	2000	800	155	<3.8	>3.8	>3.8	orbital	2800
KAIROS	0	1769	522	245		<3.8	>3.8	orbital		522
Kaituozhe-2	0	🟥	1000	🟥		<3.8	>3.8	orbital		1000
Kuaizhou-1	0	621	686	183		<3.8	>3.8	orbital		686
Kuaizhou-11	0	7530	1490	520		<3.8	>3.8	orbital		1490
LauncherOne	0	3000	250			3.4	orbital			0
Long March (CZ) 11	0	5000	🟥	500	🟥	<3.8	<3.8	>3.8	orbital	500
Long March (CZ) 12	0	10000	🟥			<3.8	orbital			0
Long March (CZ) 2C	0	10150	5143			1.9	orbital			0
Long March (CZ) 2C (SMA and YZ-1S)	0	10150	5143	🟩		1.9	7.9	orbital		5143
Long March (CZ) 2D	0	10443	4019			2.7	orbital			0
Long March (CZ) 2D/YZ-3	0	10443	4019	🟥		2.7	7.9	orbital		4019
Long March (CZ) 2F	13696	10165	8338			2.2	orbital			0
Long March (CZ) 3A	0	11021	5773	4743		<3.8	>3.8	orbital		5773
Long March (CZ) 3B and 3B/E	13696	11021	5773	4743		2.6	5.0	orbital		5773
Long March (CZ) 3B/YZ-1	13696	11021	5773	4743	🟥	2.6	5.0	9.3	orbital	10515
Long March (CZ) 3C and 3C/E	6400	10300	5395	4432		1.9	4.2	orbital		5395
Long March (CZ) 3C/YZ-1	6400	10300	5395	4432	🟥	<3.8	<3.8	>3.8	orbital	4432
Long March (CZ) 4B	0	10632	3159	3460	1488	2.1	4.6	orbital	4.2 (PF)	4646
Long March (CZ) 4C	0	10290	3041	3331	1488	2.1	4.7	orbital	4.3 (PF)	4528
Long March (CZ) 5	50310	19135	10665			6.3	orbital			19135
Long March (CZ) 5/YZ-2	50310	19135	10665	🟥		6.3	10.1	orbital		29800
Long March (CZ) 5B	51480	25612				orbital				0

Carpenter Technology Corporation (1989). *CarTech CTX-909 Alloy*. Carpenter Technology Corporation.

Carpenter Technology Corporation (1990). *CarTech CTX-3 Alloy*. Carpenter Technology Corporation.

Carpenter Technology Corporation (1994). *CarTech CTX-1 Alloy*. Carpenter Technology Corporation.

Carpenter Technology Corporation (2009). *Pyromet Alloy 718*. Carpenter Technology Corporation.

Carrillo-Sánchez, J. D., Gómez-Martín, J. C., Bones, D. L. et al. (2020). Cosmic dust fluxes in the atmospheres of earth, mars, and venus. *Icarus*, *335*, 113395. doi:`https://doi.org/10.1016/j.icarus.2019.113395`.

Chawla, K. (2001). Glass fibers. In K. J. Buschow, R. W. Cahn, M. C. Flemings, B. Ilschner, E. J. Kramer, S. Mahajan, & P. Veyssière (Eds.), *Encyclopedia of Materials: Science and Technology* (pp. 3541–3545). Oxford: Elsevier. doi:`https://doi.org/10.1016/B0-08-043152-6/00630-6`.

Daken Chemical (2024). Bisphenol A Cyanatester. `https://www.dakenchem.com/de/bisphenol-a-cyanatester-3-toxizitaetsmythen-fuer-eine-sichere-ha`

Table 7. *continued.*

Rocket	Stage mass (kg)					Stage re-entry velocity at 100 km (km/s)				Total re-entry mass with v>3.8 km/s (kg)
Stage #	0	1	2	3	4	1	2	3	4	
Long March (CZ) 6	0	8000	3000	1000		<3.8	>3.8	orbital		3000
Long March (CZ) 6A	4800	8000	3000	1000		<3.8	>3.8	orbital		3000
Long March (CZ) 6C	0	8000	🟥			<3.8	orbital			0
Long March (CZ) 7	24000	12000	🟥			>3.8	orbital			12000
Long March (CZ) 7/YZ-1A	24000	12000	6000	🟥		<3.8	>3.8	orbital		6000
Long March (CZ) 7A	24000	12000	6000	2800		<3.8	>3.8	orbital		6000
Long March (CZ) 8 and 8A	12000	12000	2800			>3.8	orbital			12000
Minotaur 1	0	2292	795	404	153	<3.8	<3.8	>3.8	orbital	404
Minotaur-4	0	3610	3190	645	256	<3.8	<3.8	>3.8	orbital	645
Minotaur-4 Orion-38	0	3610	3190	645	410	<3.8	<3.8	>3.8	orbital	645
NK Kerolox LV	0	🟥	1000	🟥		<3.8	>3.8	orbital		1000
New Glenn	0	110000	🟥			lands	orbital			0
Nuri	0	16000	4400	1290		<3.8	>3.8	orbital		4400
PSLV (all types)	🟩	30100	5350	900	670	<3.8	4.0	6.1	orbital	6250
Pegasus XL	0	1386	416	108		2.3	5.6	orbital		416
Proton-M	0	30600	11000	3500		<3.8	4.6	orbital		11000
Proton-M (Briz-M and DM-3)	0	30600	11000	3500	2370	<3.8	4.6	7.3	orbital	14500
Qaem-100	0	3030	465	🟥		<3.8	>3.8	orbital		465
Qased	0	2700	200	133		<3.8	>3.8	orbital		200
Rokot-KM	0	🟥	1500	🟥		<3.8	5.9	orbital		1500
SS-520	0	400	111	8		<3.8	>3.8	orbital		111
SSLV	0	10500	2650	1450	150	2.1	4.1	7.6	orbital	4100
Safir	0	3030	465			<3.8	orbital			0
Shavit and Shavit 2	0	1240	1376	684		<3.8	>3.8	orbital		1376
Shuang Quxian-1 and 1A	0	1744	974	282	300	<3.8	<3.8	>3.8	orbital	282
Simorgh	0	12700	1600	230		<3.8	>3.8	orbital		1600
Soyuz-2-1A	15136	6545	2410			4.3	orbital			6545
Soyuz-2-1A (Fregat, Fregat-M and Volga)	15136	6545	2410	🟩		3.9	7.0	orbital		8955
Soyuz-2-1B	15136	6545	2710			4.3	orbital			6545
Soyuz-2-1B (Fregat and Fregat-M)	15136	6545	2355	🟩		3.9	7.0	orbital		8900
Soyuz-2-1V	0	9300	2355			<3.8	orbital			0
Soyuz-2-1V Volga	15136	9300	2355	890		<3.8	>3.8	orbital		2355
Soyuz-FG	15136	6545	🟩			3.9	orbital			6545
Soyuz-ST-A Fregat-M and ST-B Fregat-MT	15136	6545	2470	🟩		3.9	7.0	orbital		9015
Soyuz-U and Soyuz-U PVB	15136	6545	2410			4.3	orbital			6545
Space Launch System - Block 1 Crew	198600	99300	3700			8.3	orbital			99300
Starship	0	220000	120000			lands	orbital			0
Starship V2	0	220000	127200			lands	orbital			0
Taurus	0	4450	1700	420	126	1.6	3.9	7.1	orbital	2120
Tianlong 2	0	9300	2355	890		<3.8	>3.8	orbital		2355
Unha-3	0	8000	1000	900		2.8	5.4	orbital		1000
Vega	0	8533	2486	1433	688	<3.8	4.0	7.6	orbital	3919
Vega C	0	13393	4238	1433	698	<3.8	4.6	7.6	orbital	5671
Vulcan Centaur VC2S	10400	50000	5500			3.3	orbital			0
Zenit-3F	0	33900	9300	1050		<3.8	>3.8	orbital		9300
Zhongke 1A	0	13393	4238	1433	698	<3.8	>3.8	>3.8	orbital	5671
Zhuque-1	0	🟥	500	🟥		<3.8	>3.8	orbital		500
Zhuque-2	0	19700	1392			<3.8	orbital			0

[Accessed 25-07-2025].

De Persis, C., & Lemmens, S. (2024). An overview of the destructive re-entry analysis tools available in europe: State of the art, latest advances, and open points. *Journal of Space Safety Engineering*, *11*(1), 35–43. doi:`https://doi.org/10.1016/j.jsse.2023.11.009`.

DOW CORNING (2011). *Material Safety Data Sheet DOW CORNING(R) 997 VARNISH*. DOW CORNING.

Drolshagen, G., Koschny, D., Drolshagen, S. et al. (2017). Mass accumulation of earth from interplanetary dust, meteoroids, asteroids and comets. *Planetary and Space Science*, *143*, 21–27. doi:`https://doi.org/10.1016/j.pss.2016.12.010`. SI:Meteoroids 2016.

Dudley, G., & Verniolle, J. (1997). *Secondary Lithium Batteries for Spacecraft*. Technical Report ESA Bulletin Nr. 90 European Space Agency.

Dumon, J., Constant, E., Spel, M. et al. (2022). Rebuild and data exploitation of the avum re-entry event for break-up model development.

Eaglepicher Technologies (2022). *Orbiter battery*. Eaglepicher Technologies Joplin, Missouri, USA.

Eames, A. (2014). Another Iridium NEXT Milestone Achieved With Successful Qualification of Its Unique Solar Panel Power System. `https://investor.iridium.com/09-23-2014-another-iridium-next-milestone-achieved-with-successful` [Accessed 25-07-2025].

ECSS Secreteriat (2019). *Space product assurance* . Technical Report ECSS-Q-ST-70-71C Rev.1 ESA Requirements and Standards Division.

Ehrlich, G. M. (2001). Lithium-ion batteries. In *Handbook of batteries* chapter 35.

Ellis, D. L. (2005). *GRCop-84: A High-Temperature Copper Alloy for High-Heat-Flux Applications*. Technical Report NASA/TM—2005-213566 NASA.

ELSOLD (). *Tin/Lead Cored Solder wires for Electronics*. ELSOLD GmbH & Co. KG Ilsenburg, Germany.

Emerson & Cuming Microwave Products, Inc. (2011). *Material Safety*

Table 8. Average elemental mass composition estimates of the different types of space waste. Elements marked green reflect the uncertainty levels described in Section 2.4; green implies a 3σ-uncertainty equal to 40% of the elemental mass fraction, yellow 80%. Elements with very high uncertainty are summarized under "Others". Values are given in %.

Element	Satellite	Average upper stage	Falcon 9/Heavy upper stage	Starship upper stage	Core stage
H	1.50	0.88	0.72	0.22	0.61
Li	0.27	0.08	0.35	0.02	0.08
Be	0.01	0.00	0.00	0.00	0.00
B	0.10	0.03	0.03	0.02	0.02
C	24.11	15.07	10.01	4.43	11.22
N	0.90	0.83	0.68	0.34	0.72
O	8.87	4.40	3.56	4.81	3.04
F	2.36	0.41	0.39	0.23	0.28
Na	0.06	0.00	0.00	0.00	0.00
Mg	1.18	0.36	0.39	0.06	0.28
Al	35.99	49.63	57.78	5.32	50.69
Si	2.81	1.61	1.49	3.99	1.41
P	0.34	0.04	0.04	0.04	0.03
S	0.02	0.01	0.01	0.01	0.01
Cl	0.06	0.04	0.03	0.01	0.03
K	0.06	0.00	0.00	0.00	0.00
Ca	0.19	0.10	0.10	0.06	0.07
Ti	4.33	4.34	4.11	3.11	3.62
V	0.15	0.21	0.18	0.13	0.18
Cr	0.60	1.90	0.99	13.15	2.69
Mn	0.10	0.23	0.23	0.66	0.26
Fe	2.92	7.48	4.32	46.28	9.91
Co	0.83	0.66	1.04	0.68	0.74
Ni	1.30	2.60	2.73	10.17	4.15
Cu	6.87	5.99	4.81	4.03	6.82
Zn	1.00	1.05	0.79	0.05	0.75
Ga	0.01	0.00	0.00	0.00	0.00
Ge	0.48	0.00	0.00	0.00	0.00
As	0.01	0.00	0.00	0.00	0.00
Br	0.19	0.12	0.12	0.07	0.08
Zr	0.03	0.05	0.08	0.01	0.06
Nb	0.00	0.57	3.33	1.06	1.06
Mo	0.03	0.11	0.10	0.20	0.20
Ag	0.81	0.07	0.14	0.04	0.07
In	0.00	0.00	0.00	0.00	0.00
Sn	0.86	0.54	0.52	0.31	0.38
Ba	0.08	0.02	0.02	0.01	0.01
La	0.00	0.00	0.00	0.00	0.00
Ce	0.01	0.00	0.00	0.00	0.00
Hf	0.00	0.05	0.36	0.10	0.10
Ta	0.01	0.01	0.03	0.01	0.01
W	0.00	0.15	0.17	0.15	0.16
Pb	0.53	0.36	0.35	0.20	0.25
Others	0.02	0.01	0.01	0.00	0.01
Sum	100.00	100.00	100.00	100.00	100.00

Datasheet Eccostock FPH. Emerson & Cuming Microwave Products, Inc. Randolph, Massachusetts, USA.

Energietechnik Essen GmbH (). *Cronidur 30 — ein Innovationstreiber*. Energietechnik Essen GmbH Essen, Germany.

ESA (2025). Database and Information System Characterising Objects in Space (DISCOS). `https://discosweb.esoc.esa.int/`. [Accessed 20-07-2025].

ESA Space Debris Office (2025). *ESA'S ANNUAL SPACE ENVIRONMENT REPORT*. Technical Report European Space Agency.

Falle, A., Wright, E., Boley, A. et al. (2023). One million (paper) satellites. *Science*, *382*(6667), 150–152. doi:`10.1126/science.adi4639`.

Feng, W., Marsh, D. R., Chipperfield, M. P. et al. (2013). A global atmospheric

Table 9. Mass fraction of material groups and of the typical materials within each material group for an average LEO satellite. Details on the typical materials are provided in the text (Section 2.2.1).

Material group	Mass fraction of material group	Typical material	Mass fraction of typical material within material group
Aluminum and aluminum alloys	0.367	7075	0.4
		2024	0.2
		6061	0.2
		5052	0.2
CFRP	0.151	Carbon fibre + epoxy resin	0.6
		Carbon fibre + cyanate ester resin	0.4
Copper and copper alloys (not including copper in other materials	0.014	Cu	0.2
		Bronze (CDA 510)	0.2
		Ni-Al-bronze (CDA 632)	0.1
		Ni-Al-bronze (C95500)	0.1
		Brass (CDA 230)	0.1
		Brass (CDA 260)	0.1
		CuBe$_2$ coated with with 0.5% Ag and Au, each	0.2
Nickel and nickel alloys	0.005	Ni	0.5
		Invar	0.5
Titanium and titanium alloys	0.046	Ti6Al4V	0.5
		Ti3Al2.5V	0.5
Steels	0.001	4130	0.5
		4340	0.5
Stainless steels	0.032	301	1/6
		304L	1/6
		316L	1/6
		431	0.3
		A286	0.1
		17-4PH	0.1
Welding, brazing, soldering	0.011	SnPb (solder)	1.0
Miscellaneous metallic materials	0.004	AZ31B	1.0
Optical materials	0.029	BK7	1/3
		ZERODUR	1/3
		SiO$_2$	1/3
Adhesives, coatings, varnishes	0.054	Acrylate	1/3
		Silicone	1/3
		Epoxy	1/6
		Epoxy (conducting, with 80% Ag)	1/6
Adhesive tapes	0.016	Acrylate	1.0
Paints, primes, inks	0.005	Polyurethane + black carbon	0.5
		Silicone + zinc oxide	0.5
Lubricants	<0.001	MoS$_2$	0.5
		PFPE	0.5
Potting compounds, sealants, foams	0.019	Epoxy	1/3
		Silicone	1/3
		Polyurethane	1/3
Rubbers and elastomers	0.002	Viton B910	0.5
		NBR	0.5
Thermosplastics (non-adhesive tapes and foils, e. g. MLI)	0.037	PTFE	0.1
		PEEK	0.1
		PVDF	0.1
		Polyimide	7/30
		Polyolefin	7/30
		DACRON	7/30
Wires and cables	0.072	Cu	0.51
		Insulation (PTFE)	0.24
		Insulation (PFA)	0.12
		Insulation (polyimide)	0.12
		Ag	0.01
Miscellaneous non-metallic materials (e. g. ceramics)	0.010	Al$_2$O$_3$	0.25
		Si$_3$N$_4$	0.25
		AlN	0.25
		SiC	0.25
Electronics (PCBs)	0.050	After Korf et al. 2019 amended with organic elements (H, C, O)	1.0
Li-ion Batteries	0.064	Case (Al)	0.12
		Cap assembly (Cu)	0.02
		Electrolyte (LiPF$_6$)	0.25
		Positive Electrode of LCO batteries(LiCoO$_2$)	0.19
		Positive Electrode of NCA batteries (LiNi$_{0.84}$Co$_{0.12}$Al$_{0.04}$O$_2$)	0.19
		Negative electrode (C)	0.18
		Separator (PE)	0.05
Solar cells + cover glass	0.010	Silicon base solar cell (Si, Ag contact)	0.13
		Triple junction solar cell (Ge, Ga, As, In, P, Ag contact)	0.52
		Solar cell cover glass (CMX100)	0.35

model of meteoric iron. *Journal of Geophysical Research: Atmospheres*, *118*(16), 9456–9474. doi:`https://doi.org/10.1002/jgrd.50708`.

Ferreira, J. P., Huang, Z., Nomura, K.-i. et al. (2024). Potential ozone depletion from satellite demise during atmospheric reentry in the era of mega-constellations. *Geophysical Research Letters*, *51*(11), e2024GL109280. doi:`https://doi.org/10.1029/2024GL109280`. E2024GL109280 2024GL109280.

Finckenor, M. M. (2018). Materials for spacecraft. In *Aerospace Materials and Applications* (pp. 403–434). doi:`10.2514/5.9781624104893.0403.0434`.

Fischer, J.-S., & Fasoulas, S. (2024). Assessment of launch and re-entry emissions of space transportation systems and their environmental impact. doi:`10.52202/078373-0079`.

Gerding, M., Wing, R., Feng, W. et al. (2025). New li lidar observations and model simulations: A window to anthropogenic signatures. *Geophysical Research Letters*, *52*(22), e2025GL118710. doi:`https://doi.org/10.1029/2025GL118710`.

Glassmeier, K.-H., & Schulz, L. (2025). Was bleibt, ist Müll. *Physik Journal*, *24*(7), 36–41.

Gomez Martin, J. C., Ocaña, A. J., Plane, J. et al. (2025). What do we know about the chemistry of spacecraft constituent metals in the lower mesospehere-upper stratosphere? EGU General Assembly 2025, EGU25-6158. doi:`https://doi.org/10.5194/egusphere-egu25-6158`.

Goodfellow GMBH (2024). *DuPont Kapton HN PI mit 30 nm Aluminium — Metallisierte Folie*. Goodfellow GMBH Germany.

GORE (2016). *GORE Space Cables Product Portfolio*. GORE.

Grassi, L. (2017). Atmoshperic re-entry assessment ARA. In *CleanSat Industrial Days*.

Gravity Cast Pvt. Ltd. (). *Material — ANSI AA A357.0*. Gravity Cast Pvt. Ltd.

Gregersen, E. (2025a). megaconstellation. `https://www.britannica.com/technology/megaconstellation`. [Accessed 31-07-2025].

Gregersen, E. (2025b). space debris. `https://www.britannica.com/technology/space-debris`. [Accessed 21-08-2025].

GS Yuasa Lithium Power, Inc. (). *Lithium Ion Cells For Satellites – Power Optimized*. GS Yuasa Lithium Power, Inc. Roswell, Georgia, USA.

GS Yuasa Power Supply Ltd. (). *Lithium ion cell for Aerospace applications LFC 40*. GS Yuasa Power Supply Ltd. Tokyo, Japan.

Gunderson, A., Setlak, S. J., & Brown Jr., W. F. (Eds.) (2007). *Aerospace Structural Metals Handbook*. (40th ed.). CINDAS LLC.

Halchak, J. A., Cannon, J. L., & Brown, C. (2018). Materials for liquid propulsion systems. In *Aerospace Materials and Applications* (pp. 641–698). doi:`10.2514/5.9781624104893.0641.0698`.

Hanning-Lee, M. A., Brady, B. B., Martin, L. R. et al. (1996). Ozone decomposition on alumina: Implications for solid rocket motor exhaust. *Geophysical Research Letters*, *23*(15), 1961–1964. doi:`https://doi.org/10.1029/96GL01808`.

Hauchecorne, A., & Chanin, M.-L. (1980). Density and temperature profiles obtained by lidar between 35 and 70 km. *Geophysical Research Letters*, *7*(8), 565–568. doi:`https://doi.org/10.1029/GL007i008p00565`.

Henkel Corporation (2023). *Safety Data Sheet Loctite Stycast 1090 BK*. Henkel Corporation Rocky Hill, Connecticut, USA.

Henkel Limited (2015). *Safety Data Sheet according to (EC) No 1907/2006 Loctite 603*. Henkel Limited Herfordshire Hatfield, Great Britain.

Henson, G. (2018). Materials for launch vehicle structures. In *Aerospace Materials and Applications* (pp. 435–504). doi:`10.2514/5.9781624104893.0435.0504`.

Herberhold, M., Bussler, L., Sippel, M. et al. (2025). Comparison of spacex's starship with winged heavy-lift launcher options for europe. *CEAS Space Journal*, . doi:`10.1007/s12567-025-00625-8`.

Inter-Agency Space Debris Coordination Committee (2025). *IADC Space Debris Mitigation Guidelines*. Technical Report IADC-02-01 Inter-Agency Space Debris Coordination Committee. Rev. 4.

Jain, A. K. (2023). *On the Atmospheric Saliency of Space Debris Reentries: Estimating Distribution, Lifetime and Radiative Forcing of Reentry-Ablated Alumina*. Master thesis, Massachusetts Institute of Technology, Cambridge, MA.

Jain, A. K., & Hastings, D. E. (2025). Global climate effect from space debris reentry: Engineering and policy implications. *Journal of Spacecraft and Rockets*, *62*(4), 1075–1082. doi:`10.2514/1.A36069`.

Janches, D., Dyrud, L. P., Broadley, S. L. et al. (2009). First observation of micrometeoroid differential ablation in the atmosphere. *Geophysical Research Letters*, *36*(6). doi:`https://doi.org/10.1029/2009GL037389`.

Jegou, J.-P., Chanin, M.-L., Mégie, G. et al. (1980). Lidar measurements of atmospheric lithium. *Geophysical Research Letters*, *7*(11), 995–998. doi:`https://doi.org/10.1029/GL007i011p00995`.

Jonathan Goff (2006). Spacex comstac briefing. `https://selenianboondocks.com/2006/10/spacex-comstac-briefing/`. [Accessed 03-08-2025].

Kayhan, N., Shoja Razavi, R., & Choopani, S. (2012). Evaluation of two new white silicone thermal control paints under atomic oxygen. *Progress in Organic Coatings*, *74*(3), 603–607. doi:`https://doi.org/10.1016/j.porgcoat.2012.02.008`.

Kearsley, A., Graham, G., McDonnell, J. et al. (2007). The chemical composition of micrometeoroids impacting upon the solar arrays of the hubble space telescope. *Advances in Space Research*, *39*(4), 590–604. doi:`https://doi.org/10.1016/j.asr.2006.05.011`.

Kessler, D. J., & Cour-Palais, B. G. (1978). Collision frequency of artificial satellites: The creation of a debris belt. *Journal of Geophysical Research: Space Physics*, *83*(A6), 2637–2646. doi:`https://doi.org/10.1029/JA083iA06p02637`.

Kester (2016). Tin-lead (snpb) bar solder. `https://www.kester.com/products/product/tin-lead-snpb-bar-solder`. [Accessed 15-08-2025].

Klinkrad, H. (2006). *Space Debris: Models and Risk Analysis*. Springer Berlin Heidelberg.

Korf, N., Løvik, A. N., Figi, R. et al. (2019). Multi-element chemical analysis of printed circuit boards – challenges and pitfalls. *Waste Management*, *92*, 124–136. doi:`https://doi.org/10.1016/j.wasman.2019.04.061`.

Krebs, G. D. (2025). Gunter's Space Page. `https://space.skyrocket.de/`. Accessed 20-07-2025.

L3Harris Technologies, Inc. (2025). RL10 Engine. `https://www.l3harris.com/all-capabilities/rl10-engine`. [Accessed 02-08-2025].

Lecadre-Scotto, A., Inguimbert, C., Lewandowski, S. et al. (2025). Aging model of optical signature for space paint coating under proton radiation. *Journal of Quantitative Spectroscopy and Radiative Transfer*, *345*, 109561. doi:`https://doi.org/10.1016/j.jqsrt.2025.109561`.

Lerch, B. A. (2018). *Properties of 5052 Aluminum for Use as Honeycomb Core in Manned Spaceflight*. Technical Report NASA/TM-2018-219753 NASA.

Li, J., Aierken, A., Liu, Y. et al. (2021). A brief review of high efficiency iii-v solar cells for space application. *Frontiers in Physics*, *Volume 8 - 2020*. doi:`10.3389/fphy.2020.631925`.

Lin, T.-N., Santiago, S. R. M. S., Zheng, J.-A. et al. (2016). Enhanced conversion efficiency of iii–v triple-junction solar cells with graphene quantum dots. *Scientific Reports*, *6*(1), 39163. doi:`10.1038/srep39163`.

Lips, T., Huertas, I., Ventura, S. et al. (2013). Results of the IAASS re-entry analysis test campaign 2012. In *Safety is Not an Option, Proceedings of the 6th IAASS Conference* (p. 89). volume 715.

Lodders, K., Bergemann, M., & Palme, H. (2025). Solar system elemental abundances from the solar photosphere and ci-chondrites. *Space Science Reviews*, *221*(2), 23. doi:`10.1007/s11214-025-01146-w`.

Lohn, P. D., Wong, E. Y., Molina, M. J. et al. (1994). *The Impact of Deorbiting Space Debris on Stratospheric Ozone*. Technical Report TRW Space & Electronics Group.

LORD Corporation (2013). *MATERIAL SAFETY DATA SHEET AEROGLAZE Z306 FLAT BLACK*. LORD Corporation Cary, North Carolina, USA.

Maloney, C. M., Portmann, R. W., Ross, M. N. et al. (2025). Investigating the potential atmospheric accumulation and radiative impact of the coming increase in satellite reentry frequency. *Journal of Geophysical Research: Atmospheres*, *130*(6), e2024JD042442. doi:`https://doi.org/10.1029/2024JD042442`.

Mangan, T. P., Harman-Thomas, J. M., Lade, R. E. et al. (2020). Kinetic study of the reactions of alo and oalo relevant to planetary mesospheres. *ACS Earth and Space Chemistry*, *4*(11), 2007–2017. doi:`10.1021/acsearthspacechem.0c00197`.

McDowell, J. C. (2025a). Enormous ('Mega') Satellite Constellations. `https://planet4589.org/space/con/conlist.html`. [Accessed 20-07-2025].

McDowell, J. C. (2025b). GCAT: General Catalog of Artificial Space Objects. `https://planet4589.org/space/gcat/index.html`. [Accessed 20-07-2025].

McDowell, J. C. (2025c). Space Object Reentries. `https://planet4589.org/space/reentry/index.html`. [Accessed 20-07-2025].

Meier, C. (2021). *Neue Hochtemperatur-Matrixharze für Kohlenstofffaser-Verbundwerkstoffe*. Ph.D. thesis Fachbereich Chemie, Technische Universität Darmstadt.

Metalcor GmbH (2025a). Datenblatt 1.4550 AISI 347. `https://www.metalcor.de/datenblatt/39/`. [Accessed 03-08-2025].

Metalcor GmbH (2025b). Datenblatt 2.1247 CuBe. `https://www.metalcor.de/datenblatt/137/`. [Accessed 28-07-2025].

Metzler, N., Dantonello, K., Roßmeier, M. et al. (2016). Influence of plasma activation on surface energy and adhesive properties of rtm6-cfrp. *Journal Of Materials Science and Surface Engineering*, *4*, 472–482.

Miraux, L. (2022). Environmental limits to the space sector's growth. *Science of The Total Environment*, *806*, 150862. URL: `https://www.sciencedirect.com/science/article/pii/S0048969721059404`. doi:`https://doi.org/10.1016/j.scitotenv.2021.150862`.

Miraux, L., Wilson, A. R., & Dominguez Calabuig, G. J. (2022). Environmental sustainability of future proposed space activities. *Acta Astronautica*, *200*, 329–346. doi:`https://doi.org/10.1016/j.actaastro.2022.07.034`.

Mitchell et al. (2024). *Whitepaper — Understanding the Atmospheric Effects from Spacecraft Re-entry*. Technical Report European Space Agency.

Molina, M. J., Molina, L. T., Zhang, R. et al. (1997). The reaction of clono2 with hcl on aluminum oxide. *Geophysical Research Letters*, *24*(13), 1619–1622. doi:`https://doi.org/10.1029/97GL01560`.

MT Aerospace (). *Spacecraft Propellant Tanks*. MT Aerospace.

Mumby, S. J. (1989). An overview of laminate materials with enhanced dielectric properties. *Journal of Electronic Materials*, *18*(2), 241–250. doi:`10.1007/BF02657415`.

Murphy, D. M., Abou-Ghanem, M., Cziczo, D. J. et al. (2023). Metals from spacecraft reentry in stratospheric aerosol particles. *Proceedings of the National Academy of Sciences*, *120*(43), e2313374120. doi:`10.1073/pnas.2313374120`.

Nammo (U.K.) Limited (). *Spacecraft Cold Gas Thruster Valve*. Nammo (U.K.) Limited Cheltenham, UK.

National Starch & Chemical Company (2004). *Eccobond 56 C*. National Starch & Chemical Company Westerloo, Belgium.

Newport Glass Works, Ltd. (2015a). Material safety data sheet BK-7 optical glass. `http://newportglass.com/amsbk7.htm`. [Accessed 01-08-2025].

Newport Glass Works, Ltd. (2015b). Material safety data sheet Ceramic Glass (e.g., ZERODUR. `http://newportglass.com/amscergl.htm`. [Accessed 01-08-2025].

NuSil Technology LLC (2009). *Material Safety Datasheet CV-1143*. NuSil Technology LLC Carpinteria, California, USA.

Oliveira, D. M., Zesta, E., & Garcia-Sage, K. (2025). Tracking reentries of starlink satellites during the rising phase of solar cycle 25. *Frontiers in Astronomy and Space Sciences*, *Volume 12 - 2025*. doi:`10.3389/fspas.2025.1572313`.

Oliveira, M. S., Mello, S. A. C., da Silva Sobrinho, A. S. et al. (2010). Surface modification of epdm rubber by microwave excited plasmas. *Surface Engineering*, *26*(7), 519–524. doi:`10.1179/174329409X446304`.

Ott, A., & Bonnal, C. (2025). Atmospheric re-entry of orbital objects – can "design for non-demise" be the optimal solution? *Acta Astronautica*, *236*, 1296–1304. doi:`https://doi.org/10.1016/j.actaastro.2025.08.002`.

Pardini, C., & Anselmo, L. (2025). Orbital re-entries of human-made space objects: Drawbacks for the upper atmosphere and the safety of people. *Journal of Space Safety Engineering*, *12*(2), 274–283. doi:`https://doi.org/10.1016/j.jsse.2025.04.009`.

Park, S.-H., Navarro Laboulais, J., Leyland, P. et al. (2021). Re-entry survival analysis and ground risk assessment of space debris considering by-products generation. *Acta Astronautica*, *179*, 604–618. doi:`https://doi.org/10.1016/j.actaastro.2020.09.034`.

Park Aerospace Corp. (2019). *F-502 Phenolic Prepregs*. Park Aerospace Corp.

Pathak, A. D., Saha, S., Bharti, V. K. et al. (2023). A review on battery technology for space application. *Journal of Energy Storage*, *61*, 106792. doi:`https://doi.org/10.1016/j.est.2023.106792`.

pauly Stahlhandel GmbH & Co. KG (2025). Werkstoff 4340. `https://pauly-stahlhandel.com/de/aisi-sae/4340`. [Accessed 28-07-2025].

Plane, J. M. C., Daly, S. M., Feng, W. et al. (2021). Meteor-ablated aluminum in the mesosphere-lower thermosphere. *Journal of Geophysical Research: Space Physics*, *126*(2), e2020JA028792. doi:`https://doi.org/10.1029/2020JA028792`.

QIOPTIQ (). *Solar Cell Coverglasses*. QIOPTIQ.

Raymond, N., Bernath, P., Boone, C. et al. (2025). Twenty years of global stratospheric fluorine inventories from atmospheric chemistry experiment fourier transform spectrometer (ace-fts) measurements. *Journal of Geophysical Research: Atmospheres*, *130*(15), e2024JD042298. doi:`https://doi.org/10.1029/2024JD042298`.

de Rooij, A. (). SPACEMATDB - Space Materials Database. Material selection. `https://www.spacematdb.com/spacemat/`. [Accessed 24-07-2025].

Ryan, R. G., Marais, E. A., Balhatchet, C. J. et al. (2022). Impact of rocket launch and space debris air pollutant emissions on stratospheric ozone and global climate. *Earth's Future*, *10*(6), e2021EF002612. doi:`https://doi.org/10.1029/2021EF002612`.

Saft (2020). *Saft solution for LEO and small GEO applications*. Saft Poitiers, France.

Schulz, L., & Glassmeier, K.-H. (2021). On the anthropogenic and natural injection of matter into earth's atmosphere. *Advances in Space Research*, *67*(3), 1002–1025. doi:`https://doi.org/10.1016/j.asr.2020.10.036`.

Schulz, L., Glassmeier, K.-H., Mitchell, A. et al. (2025). An update of space waste matter injection into the atmosphere. EGU General Assembly 2025, EGU25-6252. doi:`https://doi.org/10.5194/egusphere-egu25-6252`.

Schulz, L., Glassmeier, K.-H., Mitchell, A. et al. (2024). Space waste: An update on the natural vs human-made mass influx to the atmosphere. AGU 2024 A07-89.

Schumacher Titan (). *Ti-5Al-2.5Sn (Grade 6)*. Schumacher Titan.

Service Steel Aerospace Corp. (). *9310 ALLOY STEEL – AMS 6265 VAR – UNS93106 DATA SHEET*. Service Steel Aerospace Corp. Seattle, Washington, USA.

SGL Technic LLC (2025). *Carbonized rayon fabric*. SGL Technic LLC.

SHARP (2023). *Sharp Space Solar Cell (Standard triple-junction*. SHARP Osaka, Japan.

Shu, M., Li, Z., Man, Y. et al. (2016). Surface modification of poly (4,4"-oxydiphenylene pyromellitimide) (kapton) by alkali solution and its applications to atomic oxygen protective coating. *Corrosion Science*, *112*, 418–425. doi:`https://doi.org/10.1016/j.corsci.2016.08.009`.

Shutler, J. D., Yan, X., Cnossen, I. et al. (2022). Atmospheric impacts of the space industry require oversight. *Nature Geoscience*, *15*(8), 598–600. doi:`10.1038/s41561-022-01001-5`.

SLM Solution Group Ag (2019). *Material Data Sheet Ti-Alloy Ti6Al4V ELI (Grade 23) / 3.7165 / B348 / F136*. SLM Solution Group Ag Lübeck, Germany.

Smith, T. W., Edwards, J. R., & Pilson, D. (1999). *Summary of the impact of launch vehicle exhaust and deorbiting space and meteorite debris on stratospheric ozone*. Technical Report TRW Space & Electronics Group.

Smiths Advanced Metals (). *Radiometal 4550*. AK Steel Corporation Cambridgeshire, UK.

SpaceX (2024). Starship's third flight test. `https://x.com/i/broadcasts/1LyxBnOvzvOxN`. [Accessed 03-08-2025].

Special Metals Corporation (2004a). *INCOLOY alloy 903*. Special Metals Corporation New Hartford, New York, USA.

Special Metals Corporation (2004b). *INCONEL alloy X-750*. Special Metals Corporation New Hartford, New York, USA.

Special Metals Corporation (2006). *INCONEL alloy 625*. Special Metals Corporation New Hartford, New York, USA.

Special Metals Corporation (2008). *INCONEL alloy 600*. Special Metals Corporation New Hartford, New York, USA.

Stahlhandel Gröditz GmbH (). *17-4PH/1.4542/1.4548* . Stahlhandel Gröditz GmbH.

Steckel, G. L., & Adams, P. M. (2018). *Evaluation of Reentry Effects of Delta II Second Stage Propellant Tanks*. Technical Report TOR-2018-00670 The Aerospace Corporation.

Stiles, R. (2003). High temperature reusable surface insulation. `https://govinfo.library.unt.edu/caib/photos/viewceb7.html-photo_id=508.htm`. [Accessed 03-08-2025].

Sun, H., Guo, G., Memon, S. A. et al. (2015). Recycling of carbon fibers from carbon fiber reinforced polymer using electrochemical method. *Composites Part A: Applied Science and Manufacturing*, *78*, 10–17. doi:`https://doi.org/10.1016/j.compositesa.2015.07.015`.

Sutton, G. P., & Biblarz, O. (2017). *Rocket propulsion elements*. (9th ed.). John Wiley & Sons.

thyssenkrupp Materials Services GmbH (2018). *Material Data Sheet Aluminium alloy*. thyssenkrupp Materials Services GmbH Essen, Germany.

Tizón, J. M., & Roman, A. (2017). A mass model for liquid propellant rocket engines. In *53rd AIAA/SAE/ASEE Joint Propulsion Conference*. doi:`10.2514/6.2017-5010`.

Toumi, R. (2019). *ATmospheric Impact of SPAcecraft Demise (ATISPADE) Final Report*. Technical Report D3-ATISPADE European Space Agency.

Trelleborg sealing solutions Germany GmbH (2025). Acrylnitril-Butadien-Kautschuk. `https://www.seals-shop.com/eu/de/support/produkt-informationen/nbr`. [Accessed 10-07-2025].

Trinh, D. V. (2018). Materials for solid rocket engines. In *Aerospace Materials and Applications* chapter 11. (pp. 609–640). doi:`10.2514/5.9781624104893.0609.0640`.

Wade, M. (2019). Encyclopdeia Astronautica. `http://www.astronautix.com/index.html`. [Accessed 03-08-2025].

Wales, P. A., Salawitch, R. J., Lind, E. S. et al. (2021). Evaluation of the stratospheric and tropospheric bromine burden over fairbanks, alaska based on column retrievals of bromine monoxide. *Journal of Geophysical Research: Atmospheres*, *126*(2), e2020JD032896. doi:`https://doi.org/10.1029/2020JD032896`.

Walsh, P. R., Duce, R. A., & Fasching, J. L. (1979). Considerations of the enrichment, sources, and flux of arsenic in the troposphere. *Journal of Geophysical Research: Oceans*, *84*(C4), 1719–1726. doi:`https://doi.org/10.1029/JC084iC04p01719`.

Wanhill, R. (2014). Aerospace applications of aluminum-lithium alloys. In N. E. Prasad, A. A. Gokhale, & R. J. H. Wanhill (Eds.), *Aluminum-Lithium Alloys* (pp. 503–535). Boston: Butterworth-Heinemann. doi:`https://doi.org/10.1016/B978-0-12-401698-9.00015-X`.

Wen, L., Wang, R., & Xu, E. (2024). Optimization and mechanism study of bonding properties of cfrp/al7075 single-lap joints by low-temperature plasma surface treatment. *Coatings*, *14*(5). doi:`10.3390/coatings14050541`.

Wertz, J., Everett, D., & Puschell, J. (2011). *Space Mission Engineering: The New SMAD*. Space technology library. Microcosm Press.

Wieland Concast (2025). C95500. `https://www.concast.com/c95500.php`. [Accessed 28-07-2025].

Wing, R., Gerding, M., Plane, J. et al. (2025). Measurement of a lithium plume from the uncontrolled re-entry of a falcon 9 rocket. *Communications Earth & Environment*, . Accepted.

Wittal, M., McCann, B., Benavides, J. et al. (2022). Ambiguity remediation in space launch vehicles with parameter uncertainties: A comparison between special euclidean group and dual quaternions. 821.

Xu, K., Brito, M., Young, C. et al. (2023). Statistical analysis and modelling of small satellite reliability. In *Proceedings of the 33rd European Safety and Reliability Conference (ESREL 2023)*.

Yamauchi, M., Christon, S., Dandouras, I. et al. (2024). Heavy molecular and metallic ions in the magnetosphere. *Space Science Reviews*, *220*(8), 82. doi:`10.1007/s11214-024-01114-w`.

Zhu, C., Tian, H., & Hao, J. (2020). Global anthropogenic atmospheric emission inventory of twelve typical hazardous trace elements, 1995–2012. *Atmospheric Environment*, *220*, 117061. doi:`https://doi.org/10.1016/j.atmosenv.2019.117061`.

Declaration of interests

☒The authors declare that they have no known competing financial interests or personal relationships that could have appeared to influence the work reported in this paper.

☐The authors declare the following financial interests/personal relationships which may be considered as potential competing interests: